NTNU
Norwegian University of
Science and Technology

Investigation of bond strength and intermetallic phases in roll bonded steel-aluminium laminates at 150°C

Including the use of nickel interlayers

Erlend Sverdrup

Materials Science and Engineering (MTMT)
Submission date: June 2018
Supervisor: Bjørn Holmedal, IMA
Co-supervisor: Ida Westermann, IMA
Siri Marthe Arbo, IMA

Norwegian University of Science and Technology
Department of Materials Science and Engineering

Preface

This master's thesis, with all of its laboratory work, was conducted at the Department of Materials Science and Technology (IMA) at the Norwegian University of Science and Technology (NTNU) during the spring of 2018.

The work reported in this thesis is based on activities within the centre for research-based innovation, SFI Manufacturing in Norway and is partially funded by the Research Counsil of Norway under contract number 237900.

I would like to thank my supervisors Professor Bjørn Holmedal, Associate Professor Ida Westermann and PhD Candidate Siri Marthe Arbo for help and guidance with this thesis. Without the strong theoretical knowledge and broad laboratory experiences they contain, my work would have been a lot more difficult. A special thanks goes out to Siri Marthe for all the hours she endured with me on lab during roll-bonding, and for always keeping the door open ready to answer any question I had.

Furthermore I would wish to thank the department staff for making the experiments possible. Chief Engineer Pål Skaret knows how most stuff works and is always ready to assist. Senior Engineer Trygve Schanche is always around when you need him, which is more ofteen than not. Senior Engineer Yingda Yu makes the Electron Microscopes work and is always available when you need to focus a sample or learn some new softwares.

June 2018, Trondheim
Erlend Sverdrup

Abstract

This master's thesis investigates intermetallic growth and metallurgical bonding in cold roll-bonded steel-aluminium laminates. Commercially pure AA1080 aluminium alloy have been roll-bonded with two different steel types, namely high-strength low-alloyed (HSLA) steel and stainless steel. The samples went through a pre-rolling procedure consisting of scrubbing in acetone, wire-brushing with a rotating steel-wire brush and heat-treatment in $185°C$ hot air for $10min$. The pre-rolling procedure aimed to clean the surface and create a work-hardened brittle layer. One series also include the use of a high purity nickel interlayer between aluminium and steel. Hardness, degree of deformation and bond-strengths were analysed and evaluated, and the samples were characterised using Light Optical Microscopy (LOM) and Scanning Electron Microscopy (SEM).

In order to study and compare the growth of intermetallic phases along the three different interfaces (Fe-Al, Fe-Ni and Al-Ni), samples cut from the same roll-bonded specimen containing Ni interlayer were heat-treated at different times and temperatures. Intermetallic phases were successfully grown in both Fe-Al and Al-Ni binary systems, and their growth rates were described by a parabolic law. Values for activation energies and pre-exponential coefficients were modelled by a best-fit approach and found in agreement with literature. Characterisitc X-rays were analysed in SEM, but intermetallic phases were not successfully quantified. It is suggested that quantification should be carried out with more powerful tools such as Transmission Electron Microscopy (TEM) and X-ray Crystallography.

Both steel types were prone to work-hardening during roll-bonding. Aluminium behaved different depending on which steel type it was roll-bonded with. Aluminium roll-bonded with low-alloyed steel experienced net recovery (both static and dynamic) whereas aluminium roll-bonded with stainless steel experienced no change in hardness (static recovery followed by work hardening).

Sammendrag

Denne masteroppgaven undersøker fremvekst av intermetalliske faser i kaldvals-sveiste stål-aluminium laminater. Ren-aluminium ble kaldvalset sammen med to forskjellige ståltyper; sterkt lav-legert konstruksjonsstål (*eng.* High-Strength Low-Alloyed (HSLA)) og rustfritt stål. Prøvene gjennomgikk en for-prosedyre før valsingen som innebar vasking i aceton, børsting med roterende stålbørste og til slutt forvarming på $185°C$ i $10 minutter$. Hensikten med prosedyren var å vaske overflatene fri for enhver forurensing, og så lage et hardt og sprøtt arbeidsherdet sjikt. Forvarmingen tjente for å myke stålet før valsing. En serie ble også produsert med et mellomsjikt av ren-nickel. Det ble gjort hardhetstester, graden av plastisk deformasjon ble undersøkt og bindingsstyrken ble testet. Prøvene ble karakterisert ved bruk av lys- (LOM) og elektronmikroskopi (SEM).

Prøver kuttet fra det samme valseproduktet med lav-legert stål, aluminium og nikkel mellomsjikt ble varmebehandlet på forskjellige tider og temperaturer for å undersøke fremveksten av intermetalliske faser. Intermetalliske faser vokste frem både i Fe-Al- og Al-Ni-systemene, og vekstraten ble beskrevet med en parabolsk lov. Aktiveringsenergiene og koeffisientene for den beskrivende ligningen ble funnet ved hjelp av en "best-egnet"-tilnærming basert på eksperimentelle data, og resultatene var i samsvar med litteraturen. Intermetalliske faser ble forsøkt kvantifisert ved hjelp av karakteristisk røntgenstråling i SEM, men uten hell. Det foreslås at kvantifisering bør foregå i transmisjonselektronmiskroskop eller røntgenkrystallografi.

Begge ståltypene gjennomgikk arbeidsherding i valseprosessen. Aluminiumen oppførte seg derimot forskjellig avhengig av hvilken ståltype den ble valset med. Aluminium som ble valset med lavlegert stål gjennomgikk netto gjenvinning (statisk og dynamisk) mens aluminiumen som ble valset med rustfritt stål ikke endret hardhet (statisk gjenvinning fulgt av arbeidsherding).

Contents

1 Introduction

Steel and aluminium are among the most important engineering metals as they are cheap, accessible and provide good mechanical properties [1]. Steels offer the customer high strength and high stiffness whereas aluminium and its alloys offer good corrosion resistance and low density. Thus, joining of these metals are of large commercial interest as a combination would offer the customer a set of properties not matched by one-type traditional materials.

Joining could either be done warm or cold, i.e. fusion welding or solid state welding. When heating one or more of the metals to a temperature above melting, properties such as strength, ductility etc. are prone to change. Making a strong joint and still keeping the mechanical properties and/or microstructure of the base materials unchanged are therefor topics of interest for many researchers.

Cold roll bonding is a solid state bonding process where sheets are welded together by plastic deformation and applied pressure. This thesis investigates cold roll bonding of commercial pure aluminium with low-alloyed and stainless steels. Bond strengths are investigated in light of deformation and metallurgical studies. Steel-aluminium joints are prone to form Fe_xAl_y intermetallic phases, which are brittle and thus often undesired. One set of samples was therefor produced with a nickel interlayer between steel and aluminium in order to avoid formation of intermetallic phases. Heat treatments are conducted to try to gain an understanding of intermetallic layer growth kinetics between Fe-Al, Fe-Ni and Al-Ni.

This thesis will first provide the reader with a theoretical introduction to roll bonding and the formation of intermetallic phases in binary systems. Next, the experimental procedures conducted are well described, and results are presented and discussed.

2 Theoretical background

This chapter aims to give the reader an introduction to cold roll bonding of steel and aluminium, as well as present state-of-the-art literature on the topic. First, the materials studied in this thesis will be briefly presented; their classification, how they can be strengthened and how they can be softened. Then an introduction to recent work on intermetallic phases will follow, before necessary theory in the fields of solid-state joining and materials characterisation round off this chapter.

2.1 Properties of metals

2.1.1 High-strength, low-alloy (HSLA) steels

High-strength, low-alloy steel is a group of low-alloyed steels but with high strength. HSLA steels contain certain alloying elements to give it desired mechanical properties, but the carbon-content is in general low. Traditionally, strengthening in steel was done by adding carbon (C) and manganese (Mn) to the steel [2]. Carbon served to increase the pearlite content (ferrite and cementite layered structure) while manganese increased the strength by going into solid solution. Although adding carbon and manganese increased the strength it also made the steel brittle and non-weldable (due to the formation of brittle martensite). Thus, HSLA steels offer high strength, good weldability and high toughness.

2.1.2 Stainless steels

Stainless steels are steels with a chromium content greater than $12wt\%$ [2]. Cr reacts with oxygen from the air to form a thin, stable oxide layer on the surface. The oxide layer prevents oxygen diffusion and further corrosion. Addition of nickel to the steel increases the corrosion resistance and makes the steel austenitic. Austenitic steels have a stable austenite phase even at room-temperature, with the austenite $\rightarrow$ martensite transition taking place below room-temperature. Due to the FCC-phase, austenitic stainless steels can undergo large amounts of extensions and work-hardening [2].

316L is a austenitic stainless steel with a Cr/Ni-content of at least $16/10wt\%$. The "L" indicates a low carbon-content, no more than $0,03wt\%$. A low carbon-content prevents formation of the damaging $Cr_{23}C_6$-phase on grain boundaries (sensitization) during heat-treatments such as welding. Molybdenum helps repair the surface oxide layer, and with nickel it also resists pitting corrosion.

2.1.3 Aluminium alloys

Aluminium is a light, ductile metal with FCC-structure. A widely regarded standard for aluminium alloy designation is the standard established by the Aluminum Association, AA. Aluminium alloys are given a four-digit number which tells what alloying elements

are present. The first digit classifies which series the alloy belong to. Table 1 lists the alloying series and respective main alloying element(s).

Table 1: Aluminum Association alloy designation [2, 3].

Series	Main alloying element(s)
1xxx	-
2xxx	Cu
3xxx	Mn
4xxx	Si
5xxx	Mg
6xxx	Mg & Si
7xxx	Zn
8xxx	other

2.1.4 Strengthening mechanisms

Strengthening of a metal occurs by decrease in dislocation mobility, that is how easily a dislocation can move in the lattice [4–6]. Dislocation mobility can be decreased by a number of mechanisms; grain size refinement, solid-solution strengthening, precipitation hardening and strain hardening (often referred to as "work hardening"). Strengthening of a metal leads to the metal becoming less ductile.

In a poly-crystalline metal, grains share grain boundaries which acts as dislocation movement barriers for two reasons. Firstly, two neighbouring grains have different orientations, and the dislocation motion therefor has to change. Secondly, the atomic disorder which is found at a grain boundary results in discontinuous slip planes resulting in a "leap" from one grain to the next. A fine-grained material has more grain boundaries than a coarse-grained one, and the strength increases with decreasing grain size following the Hall-Petch equation:

$$\sigma_y = \sigma_0 + k_y d^{-1/2} \tag{1}$$

where σ_0 and k_y are material constants and d is the average grain size diameter.

Solid-solution strengthening occurs by foreign atoms occupying vacancies in the lattice. If the solute atoms are of similar size as the base metal they will occupy lattice points in the crystal. This is called substitutional solid solution. Otherwise, if the solute atoms are much smaller than the solvent they will occupy interstitial vacancies. This is called interstitial solid solution. Solid solution works by creating a strain-field around the solute atoms due to difference in atom size.

Precipitation hardening occurs when atoms in solid solution precipitate during cooling to form a secondary phase in the lattice. In order for a precipitate to form its solubility has to decrease with decreasing temperature. Precipitates can either stop dislocations, forcing them to bypass the particle, or retarding dislocations by cleavage in which energy is absorbed.

Strain hardening is the phenomenon where a metal hardens by plastically deformation. Dislocation density increases due to dislocation multiplication and formation of new

dislocations. The average inter-dislocation length decreases and dislocation-dislocation-interactions get more common. On average, dislocation-dislocation-interactions are repellent and thus contribute to higher strength.

2.1.5 Recovery, recrystallisation and grain growth

A strain-hardened metal is in an unstable condition. By increasing the temperature the metal can be annealed, that is softened. Annealing consists of three more or less distinct processes; recovery, recrystallisation and grain growth.

During recovery dislocations move to relieve the lattice. Physical properties like electrical and thermal conductivities are recovered to their initial state (pre-worked), but mechanical properties are not affected much. In order for the strength to decrease and ductility to increase the metal has to undergo recrystallisation. Recrystallisation is the phenomenon in which a new set of strain-free grains are created at the cost of the strain-hardened and non-equilibrium state older grains. During recrystallisation the metal becomes weaker, softer and more ductile.

If kept at the same (or higher) temperature after complete recrystallisation, the metal will undergo grain growth. During grain growth, large strain-free grains will grow at the cost of smaller, less favourable, grains. Therefor the average grain size will increase, and the metal will have a range of grain sizes which is often undesirable.

The metal can also recover during plastic deformation, in which case it is called dynamic recovery (opposite to static recovery which is after deformation has occurred). During dynamic recovery, the metal hardens and recovers simultaneously, creating some sort of dynamic equilibrium [7].

2.2 Properties of intermetallics

Metals can react to form intermetallic phases, i.e. compound with metallic bonding and defined stoichiometry. They form when the solubility limit of a metal is reached and the solute reacts with the solvent to form new phases. Intermetallic phases do often have mechanical and/or chemical properties varying from the pure metals (e.g. hardness, brittleness and metling point), and joints are often limited by the formation of intermetallic phases. Thus the growth of intermetallics should be controlled by process parameters. In order to fully understand the formation of intermetallic phases, a study of the respective binary systems has to be conducted.

2.2.1 Fe-Al binary system

The Fe-Al phase diagram is shown in Figure 1. The system contains several stable intermetallic phases, namely Fe_3Al, FeAl, $FeAl_2$, Fe_2Al_5 and Fe_4Al_{13} (often shortened to $FeAl_3$). When joining in solid state most literature reports on formation of Al-rich phases, fewer on the Fe-rich intermetallics [8–10]. The Al-rich phases have the lowest effective heat of formation at the concentration of lowest eutectic, and according to the EHF-theory

(see section 2.2.4) these will form first. However, Kobayashi & Yakou [11] have studied the growth mechanisms of FeAl and Fe_3Al on coated carbon steel at temperatures above $T_{m,Al}$. As this project only takes solid Al into consideration, research on temperatures above $T_{m,Al}$ will not be bothered.

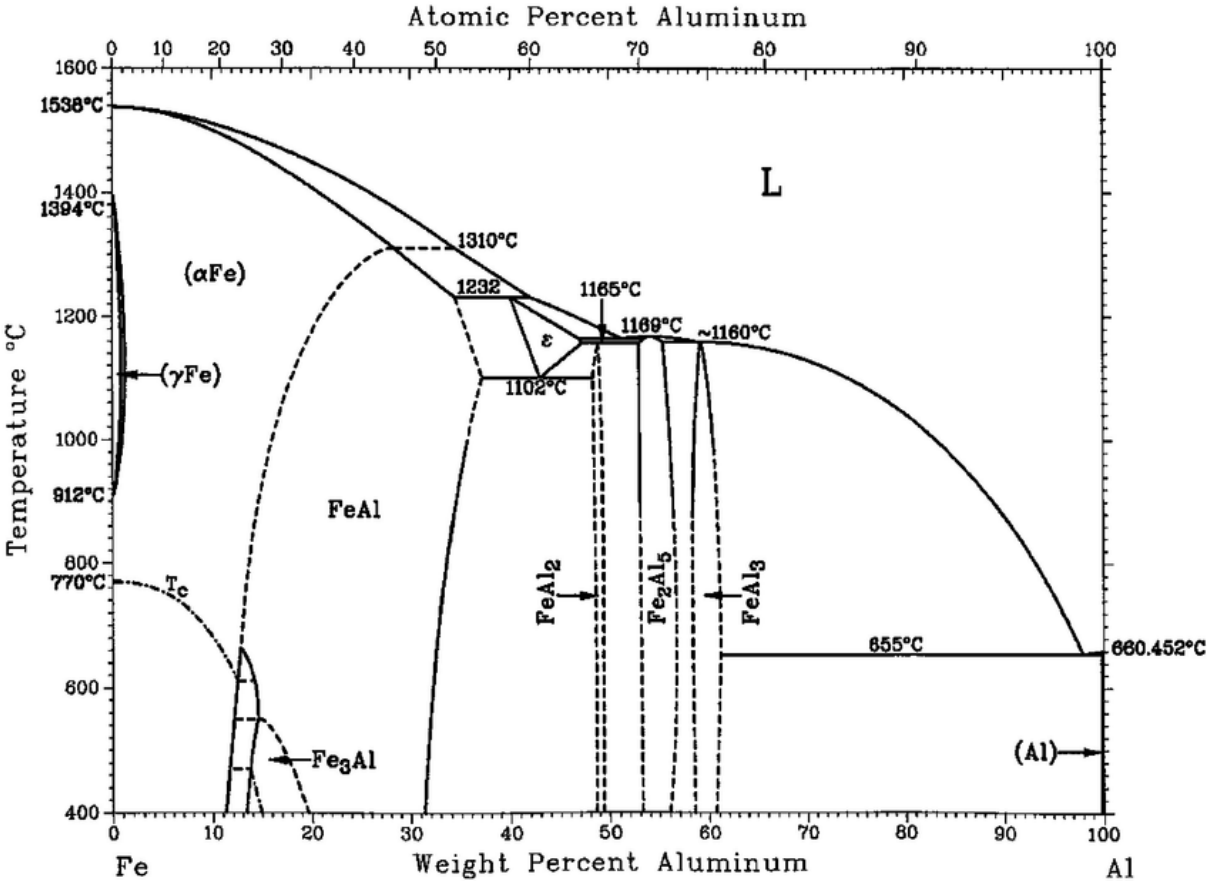

Figure 1: Fe-Al binary phase diagram [12]. Note that Fe_4Al_{13} is displayed as $FeAl_3$.

The solubility of iron in aluminium, Fe(Al), is close to zero, as can be read from the phase diagram. There is an eutectic point at approximate $98wt\%$ Al which is the lowest temperature a liquid can have in equilibrium conditions. Eutectic temperature is $655°C$. The solubility of aluminium into iron is on the other hand greater.

2.2.2 Al-Ni binary system

The Al-Ni phase diagram is shown in Figure 2. The binary system contains five stable intermetallic phases; Al_3Ni, Al_3Ni_2, AlNi, Al_3Ni_5 and $AlNi_3$. One can see from the phase diagram that the solubility of nickel into aluminium, Ni(Al), is limited (close to zero), whereas the solubility of aluminium into nickel is better ($\geq 2wt\%$). The lowest eutectic point is at approximate $92wt\%$ Al and $T = 640°C$.

Literature reports on the formation of Al_3Ni and Al_3Ni_2 on the aluminium-nickel interface [13] during heat treatment of nickel-coated aluminium substrate.

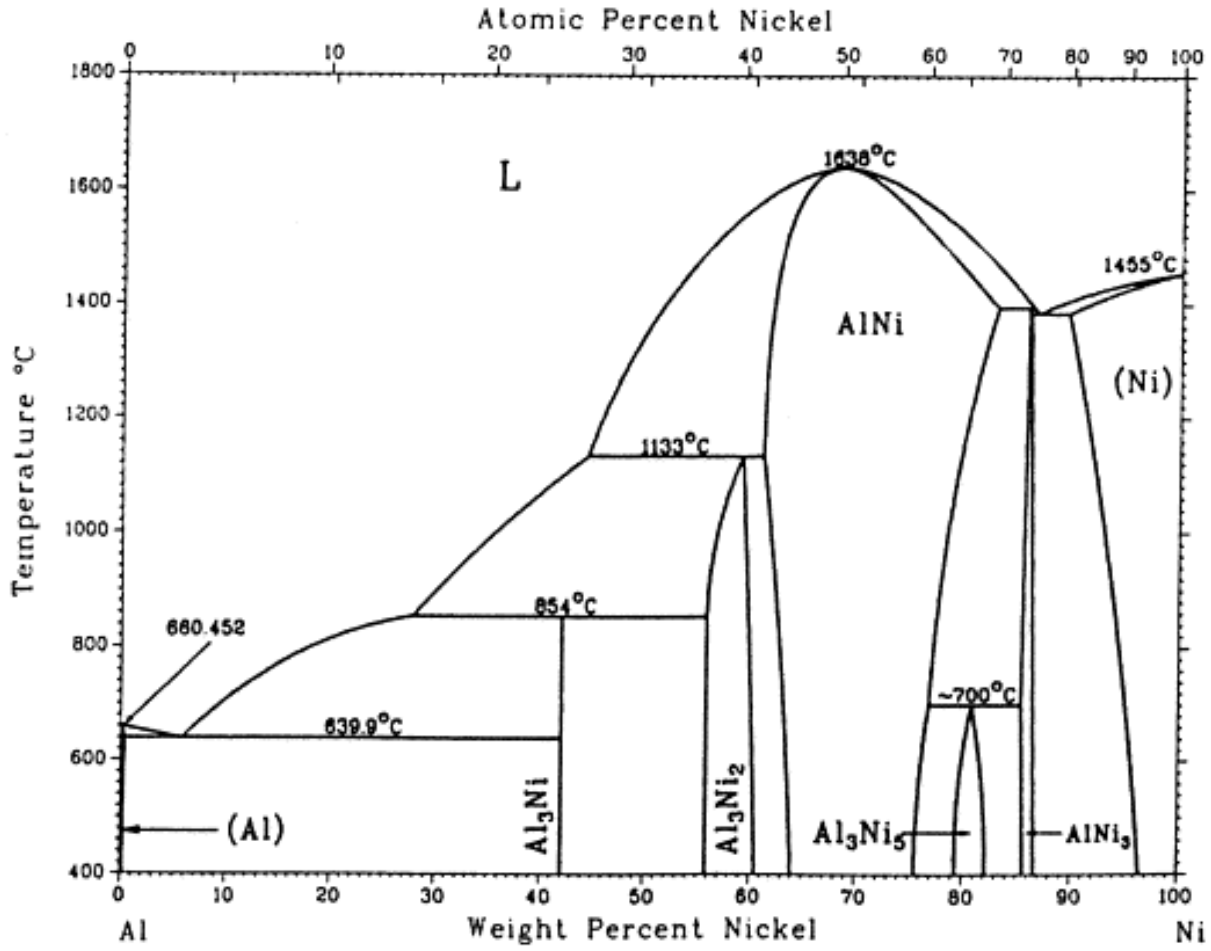

Figure 2: Al-Ni binary phase diagram [12]

2.2.3 Fe-Ni binary system

The binary Fe-Ni phase diagram is shown in Figure 3. At elevated temperatures it is complete solubility between iron and nickel. Intermetallic phases exist on lower temperatures but none which melts congruently. The lowest stable liquid phase exists at approximate $30wt\%$ Fe and $T = 1425°C$.

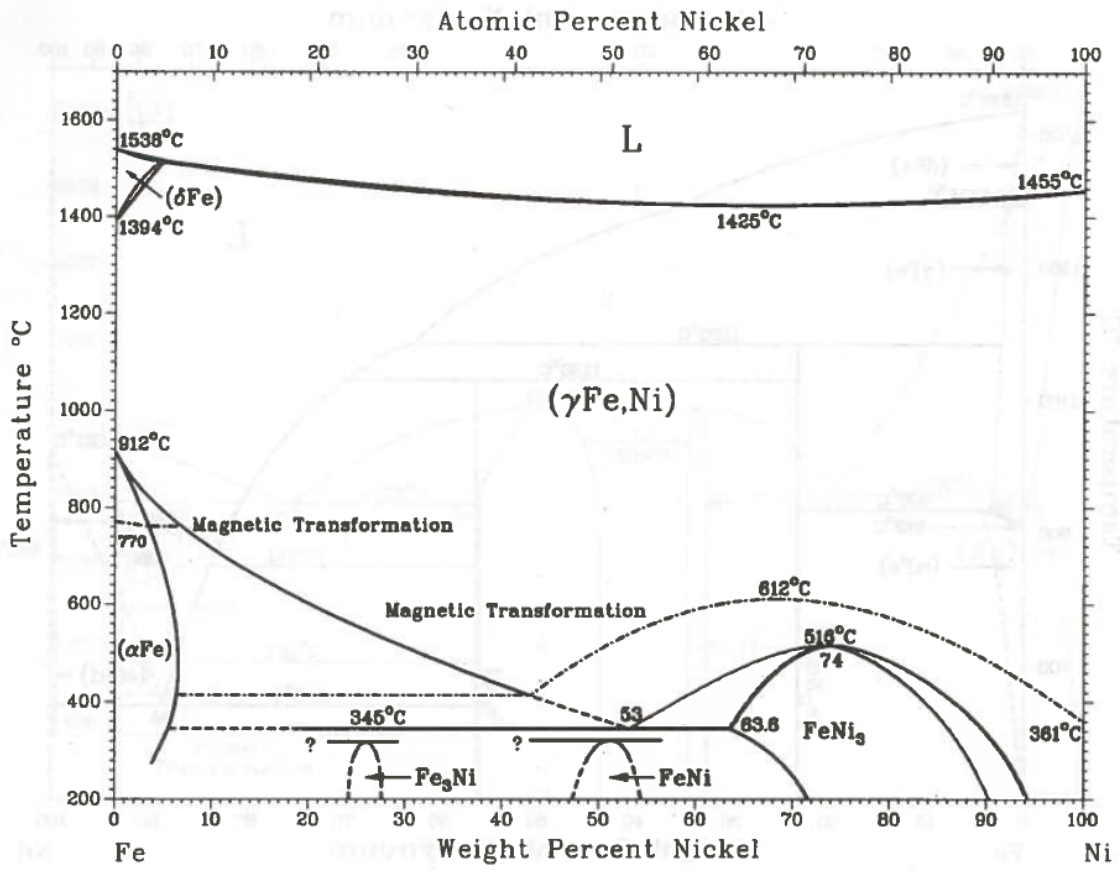

Figure 3: Fe-Ni binary phase diagram [12]

2.2.4 First-phase formation theory - Effective Heat of Formation (EHF)

The first good model to predict first-phase formation during solid state metal-metal interaction was the Walser-Bené model, generalised by Bené in 1982 [14]. It states that "*the first phase nucleated in metal-metal thin-film reactions is the phase immediatly adjacent to the low-temperature eutectic in the binary phase diagram*" [14].

Later, Pretorius builds on that theory to include thermodynamic calculations in order to predict the first-phase formation [15]. The driving force for a reaction is the change in Gibbs free energy, ΔG^0, given by Equation 2

$$\Delta G^0 = \Delta H^0 - T\Delta S^0 \tag{2}$$

where ΔH^0 is the change in enthalpy, T is the temperature in kelvin and ΔS^0 is the change in entropy. As the change in entropy for a system during a solid state reaction is negligibly small compared to the heat of formation, the expression can be simplified to

$$\Delta G^0 \approx \Delta H^0. \tag{3}$$

Heat of formation can thus be used to predict phase formations, as the system seeks the state of lowest free energy. Pretorius *et al.* [15–17] have included concentration to the enthalpy model, resulting in the Effective Heat of Formation Model (EHF). The effective heat of formation, $\Delta H'$, is defined as

$$\Delta H' = \Delta H^0 \times \frac{\text{effective concentration of limiting element}}{\text{compound concentration of limiting element}}. \tag{4}$$

The effective concentration is chosen to be that of the lowest eutectic of the binary system as the mobility of the atoms is greatest at this concentration, similar to the concentration chosen by Bené [14]. If an eutectic does not exist in the respective system, another concentration has to be chosen. For aluminium, this value tends to be 98at%Al as this is close to pure aluminium with its low melting point [17]. Compound concentration is the stochiometric concentration of the limiting element in the phase studied. Consider the following example from Pretorius *et al.* [17]:

Example: Consider the formation of $ZrAl_2$ and assume that the effective concentration of Zr at the growth interface is 50at% and 50at% for Al. The heat of formation, ΔH^0, is $-46\frac{\text{kJ}}{\text{mol at}}$, the compound to be formed is $Zr_{0,333}Al_{0,667}$ and the effective concentration is $Zr_{0,5}Al_{0,5}$. The effective heat of formation will be

$$\Delta H' = -46\frac{\text{kJ}}{\text{mol at}} \times \frac{0.5}{0.667} = -34.5\frac{\text{kJ}}{\text{mol at}}. \tag{5}$$

Theron *et al.* [18] compared the Walser-Bené and the EHF models, and found the EHF model to predict the correct first-phase in 88% of the systems studied (74 out of 84 binary systems).

The effective heats of formations for the known phases in the Al-Fe system are presented in Table 2. Iron was chosen as the limiting element in the calculations of effective heat of formation, as diffusion of iron atoms has been found to be the mechanism behind intermetallic growth. However, Wang & Vecchio [19] argues that Al diffuses into steel.

Table 2: Enthalpy values for the known phases in the Fe-Al system [18]

Phase	Composition	ΔH^0 $[\frac{\text{kJ}}{\text{mol at}}]$	$\Delta H'$ $[\frac{\text{kJ}}{\text{mol at}}]$
Fe_3Al	$Fe_{0,75}Al_{0,25}$	-22	-0.264
FeAl	$Fe_{0,5}Al_{0,5}$	-	-
$FeAl_2$	$Fe_{0,333}Al_{0,667}$	-25	-0.676
Fe_2Al_5	$Fe_{0,286}Al_{0,714}$	-22	-0.692
Fe_4Al_{13}	$Fe_{0,235}Al_{0,765}$	-19	-0.728

As can be seen in Table 2, Fe_4Al_{13} has the largest negative effective heat of formation. Theory states that this phase should be the first to form. Further, theory says that the "*next phase to form at the interface between the compound phase and remaining element is the next phase richer in the unreacted element, which has the most negative effective heat of formation*" [17]. For the Fe-Al system that will be Fe_2Al_5.

Table 3: Enthalpy values for the known phases in the Al-Ni system [20]

Phase	Composition	ΔH^0 $[\frac{\text{kJ}}{\text{mol at}}]$	$\Delta H'$ $[\frac{\text{kJ}}{\text{mol at}}]$
Al_3Ni	$Al_{0,75}Ni_{0,25}$	-41	-5,74
Al_3Ni_2	$Al_{0,6}Ni_{0,4}$	-54,5	-4,77
AlNi	$Al_{0,5}Ni_{0,5}$	-54,7	-3,83
Al_3Ni_5	$Al_{0,375}Ni_{0,625}$	-	-
$AlNi_3$	$Al_{0,25}Ni_{0,75}$	-36,6	-1,71

As for the Al-Ni system, the first phase predicted to form is Al_3Ni, followed by the growth of Al_3Ni_2 on the Al_3Ni-Ni-interface. Effective heat of formations are calculated in Table 3 based on enthalpy of formation values from Chrifi-Alaoui *et al.* [20]. Nickel acts as the limiting element in the binary system.

Even though the EHF model predicts most first-phase formations in binary systems well, it is not a perfect model. It has been shown that it struggles with systems with congruent compounds. The Fe-Al system has one congruently melting phase, namely Fe_2Al_5. Congruent phase means that it solidifies without changing composition; there is no two-phase region before complete solidification.

Laik *et al.* [21] proposed a modified EHF model that includes the heat of formation for congruent compounds;

$$\Delta H^m = (\Delta H^0 + \Delta H^f) \times \frac{C_e}{C_1} \tag{6}$$

where ΔH^f is the heat of formation for congruent compounds and zero for non-congruent compounds.

$$\Delta H^f = R \times T_m \tag{7}$$

where R is the universal gas constant and T_m is the melting point for the congruent phase.

As the EHF model is reported to predict correct first-phase formation for both Fe-Al and Al-Ni systems, the MEHF model will not be paid much attention.

2.2.5 Kinetics - Parabolic growth rate

Jindal et.al. [8] have found the growth rate of Fe_2Al_5 to be parabolic, following Equation 8

$$\frac{d\Delta x}{dt} = \frac{k}{\Delta x} \tag{8}$$

where the parabolic rate constant k is defined as the Arrhenius relation, $k = k_0 \times \exp(\frac{-Q}{RT})$. R is the gas constant, T is the temperature in kelvin, Q is the activation energy for the respective phase and k_0 is the pre-exponential factor. The equation can be re-written to state layer thickness, Δx, as a function of temperature, T:

$$\Delta x = \left[2k_0 \int_0^t \exp\left(\frac{-Q}{RT(t)}\right) dt \right]^{1/2} \tag{9}$$

Note that for a thermomechanical process the temperature will be a function of time, $T(t)$. The integral does not have an analytical solution, and thus has to be solved numerically.

Adabi & Amadeh [13] argues that the growth of both Al_3Ni and Al_3Ni_2 follows a parabolic rate. They also observed that aluminium was the dominant diffusing element during the first phase growth of Al_3Ni, while nickel was the dominant during second phase growth of Al_3Ni_2. Their work is conducted by electrodepositing of nickel onto 6061 aluminium alloy substrate.

2.3 Properties of metallic interlayer

The primary function of an interlayer is to prevent formation of brittle intermetallic layers between the two joining metals. A common material to serve as interlayer is nickel [13, 22–27]. Nickel, with its FCC structure, is ductile yet strong at both room temperature and elevated temperatures [2]. It has good corrosion resistance, and works as base for a lot of super-alloys

Literature shows that nickel interlayer does not react with either ferritic nor austenitic stainless steel types during diffusion bonding in inert atmosphere/vacuum at elevated temperatures up to $850°C$ [13, 22–27]. Zhong *et al.* [27] argues that no intermetallic phase form on the steel-nickel interface due to the high solubility of nickel in iron (Ni(Fe)) and vice versa.

2.4 Solid-state joining

Traditionally, dissimilar metals have been combined by fusion welding, meaning that a liquid phase is present during the welding process. Fusion welding can lead to chemical segregation, stress concentration and formation of brittle intermetallic layers, and an alternative method is desired. More recently solid-state joining have been investigated [8, 28, 29]. Solid-state joining means that there never is a liquid phase present; the two materials are always in solid state. Bonding can occur either by mechanical processes (e.g. riveting, clinching, seaming) or by metallurgical processes (e.g. extrusion, rolling, welding). Metallurgical bonding means that there is metal-metal interaction at the interface, whereas mechanical bonding rely on interlocking and interfacial pressure. As this thesis deal with roll-bonding of dissimilar metals (i.e. metallurgical joining), the following sections will give a brief introduction to the governing mechanisms behind metallurgical joining in general and roll-bonding in specific.

2.4.1 Metallurgical bonding

In order to obtain metallurgical bonding, fresh metal surfaces have to be in contact. For metal-metal contact to be possible, contaminating layers, oxide films and otherwise artificially constructed brittle layers have to be removed [30, 31], and high interfacial pressure has to be applied. Severe plastic deformation leads to the brittle surface layers cracking and virgin metal being extruded through to form bonding. This mechanism was

first referred to as the film theory by Mohamed & Washburn [32] and illustrated in Figure 4. A high surface pressure (exceeding yield stress of the metal) also serves to flatten out any topography present, and thereby increasing the contact area.

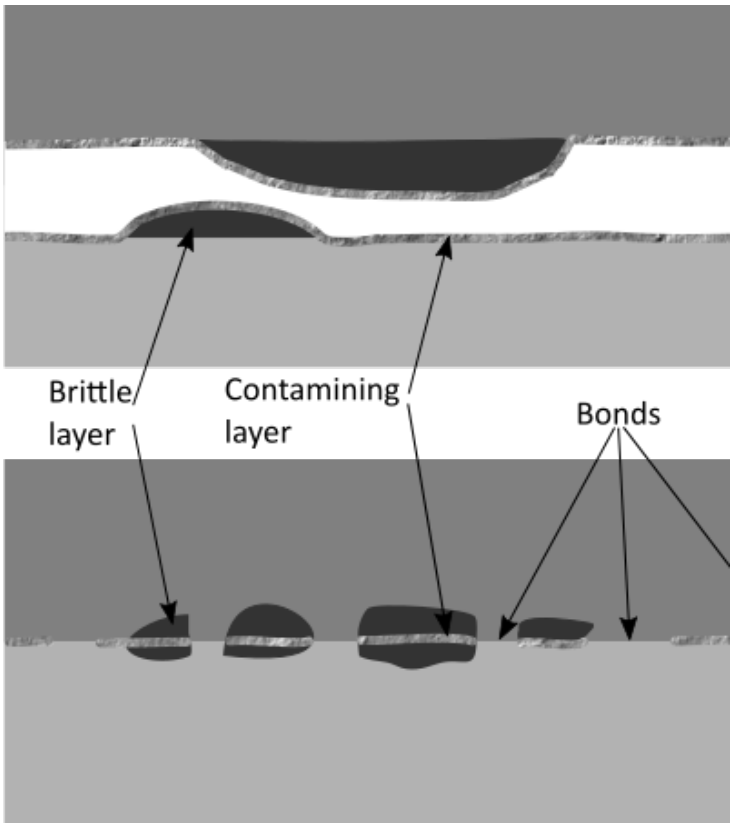

Figure 4: Illustration of the bonding mechanism according to the film theory. Hard and brittle surface layer due to work hardening is illustrated with dark colour. Sketch made by the author.

One of the most influential process parameters is the degree of plastic deformation, i.e. surface expansion/exposure. A threshold value has to be reach before bonding occurs, and by increasing the deformation further bond strength will increase [28, 33]. As surface expansion is proportional with normal pressure the pressure applied is also an important process parameter, as argued by Bay [30].

Another important parameter is surface preparation. Surface treatment prior to bonding can serve as cleaning (chemical and mechanical) or construction of a brittle layer (by work hardening). By introducing a brittle, work-hardened layer on the surface, the surface will crack open at lower strains and bond according to the film theory. Cleaning can help remove contamination on the surface. Literature shows that a combination of chemical cleaning with acetone and mechanical brushing with a steel-wire brush results in good bonding [34].

2.4.2 Cold roll bonding

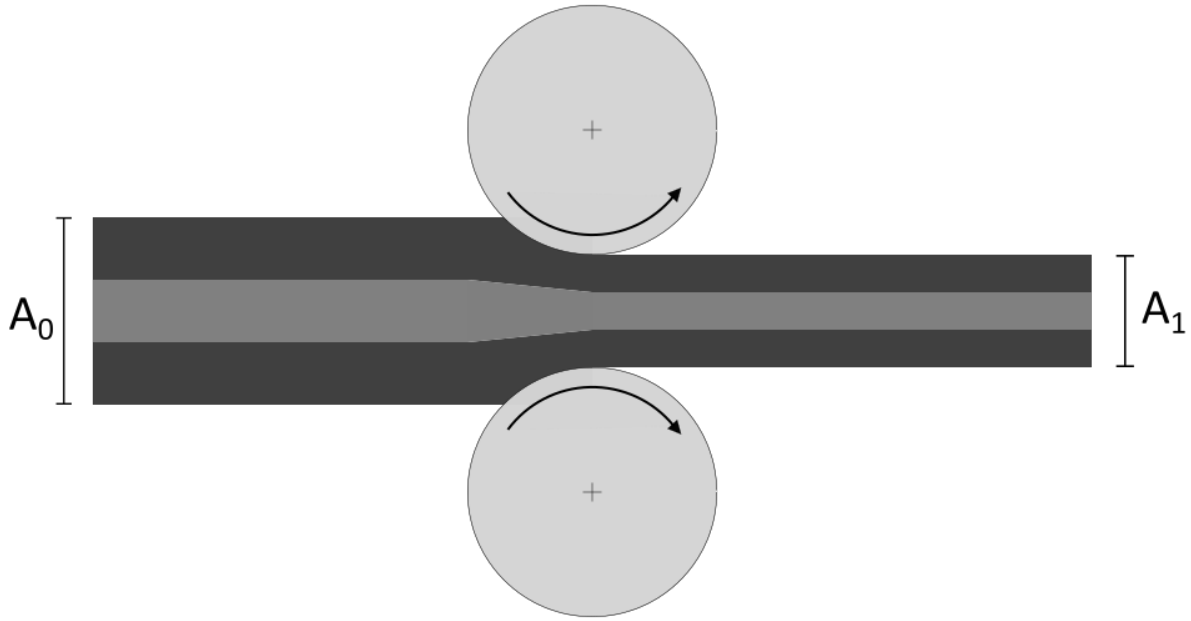

Figure 5: Illustration of the roll-bonding process as seen from the side. Different sheet layers are indicated by different colours, and the rollers are drew as circles with rolling direction indicated by arrows. Initial and final thickness are named A_0 and A_1, respectively. Sketch made by the author.

The process of cold roll bonding is illustrated in Figure 5. Stacked sheets are fed into the gap between rollers and plastically deform as they pass by. Bonding can occur as a result of the plastic deformation felt between the rollers. Cold refers to the temperature being below that of recrystallisation, opposite to warm rolling.

Bonding might occur when a metal interacts with another metal under high pressure. To obtain metal-metal interaction fresh metal surfaces have to come in contact, and surface contaminants and oxide layers have to be removed. Fresh metal is exposed when the surface cracks open and expands. Due to volume conservation, the surface expansion can be expressed in the terms of thickness reduction. If we assume that material only can flow in rolling direction and the direction of applied force from the rollers, we can express the surface expansion as

$$X = \frac{A_0 - A_1}{A_0} \tag{10}$$

where A_0 is the initial thickness and A_1 the final thickness post rolling. The higher the value of X, the higher the degree of metal-metal contact.

Flow stress, which is the stress required to continue deforming at a given strain, is inversely proportional with temperature [35]. By roll bonding at an elevated temperature, the force/stress required is thus lower than at room temperature.

2.5 Peel test

Bond strengths and adhesives can be tested by tensile, shear or peeling applied force, see Figure 6. Tensile and shear tests apply force to the whole contact area simultaneously, whereas peel tests applies force only to a cross-section of the sample. Thus, peel tests are well suited for strong bonds/adhesives.

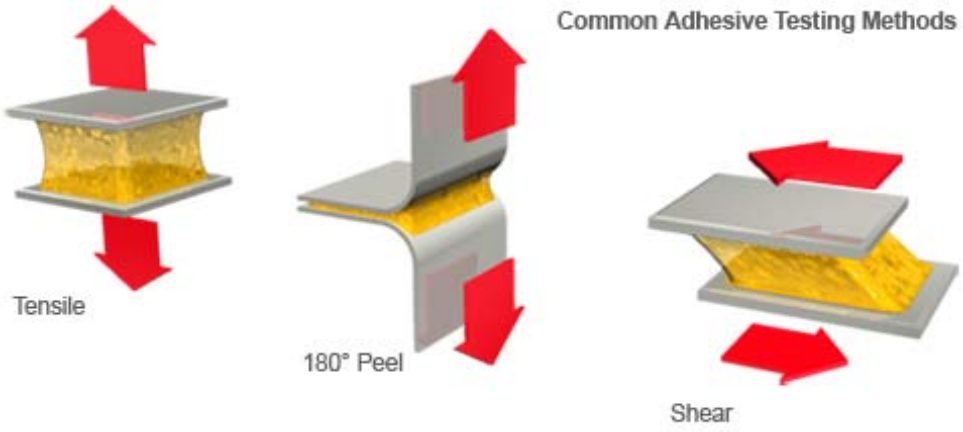

Figure 6: Illustration of three distinct bond/adhesive strength test modes; tensile, peel and shear. [2018; *http* : *//www.adhesivetest.com/peal_test.htm*]

Two commonly used peel tests are the ASTM-D1876 [36] and ASTM-D3176 [37] tests. The former peels in a "T"-set-up, the latter bends one of the layers upwards 90°. Both measure peel force, and bond strength can be calculated as

$$\text{Bond strength} = \frac{\text{Average peel force } [N]}{\text{Specimen width } [mm]} \tag{11}$$

2.6 Scanning Electron Microscopy (SEM)

Scanning Electron Microscopy (SEM) uses an electron beam to "look" at the specimen, rather than light as an ordinary light microscopy uses. Due to the significant lower wavelength of electrons compared to that of visible light, the resolution of a SEM is much higher than of a LOM (Light Optical Microscopy). The depth of field is increased compared to that of a LOM. A drawback with SEM is electrical charging of the specimen if it is not electrical conductive, or if a metallic specimen is not in direct contact with the specimen holder. A metallic specimen moulded in epoxy will not be conductive, and measurements has to be taken. Common methods to deal with a moulded specimen are (1) to wrap the specimen in graphite tape and aluminium thin-foil or (2) to remove the specimen from the mould.

2.6.1 Energy-dispersive X-ray spectroscopy - EDX/EDS

Incoming electrons, if the energy is sufficient, can excite electrons from the specimen and create vacancies in the orbitals, ionising the atom [38]. These vacancies (holes in the

orbitals) create instabilities and new electrons will automatically fill the holes. Electrons from a higher energy level will "fall down" in terms of electron shell number from high to low and create a stable atom. The energy difference in which the electron experiences is emitted as X-ray radiation. As each element has specific and discrete energy levels, emitted X-rays can be detected and used to characterise the element present.

For X-ray analysis, letter-notation is preferred. $K, L, M, M, ...$ corresponds to electron shell number $n = 1, 2, 3, 4, ...$ Electrons that fill a vacancy in the K-shell ($n = 1$) emit X-ray with the notation K, electrons that fill a vacancy in the L-shell emit X-rays with the notation L, and so on. X-rays are also given a small Greek letter in subscript, indicating from which electron shell they fell. An electron falling from the L-shell to the K-shell emits X-ray with the notation K_α, an electron falling from M to K gets the notation K_β. Figure 7 shows now notation are given X-rays emitted from electron movement.

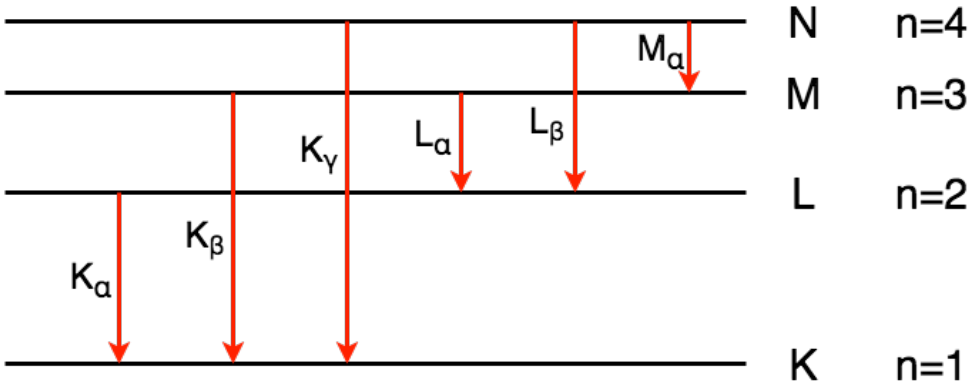

Figure 7: Illustration of the discrete atomic energy levels in which electrons can occupy vacancies. Sketch made by the author.

3 Experimental procedures

This chapter serves to describe the procedures carried out in order to produce the samples in this report. First, the materials used are presented, Secondly, the procedures of making the samples are described. Finally, the methods of mechanical testing and characterisation are presented.

3.1 Material selection

For this report, commercially pure AA1080 aluminium ($\geq 99.8 wt\% Al$) was cold bonded with two different steel types, namely a low-alloyed and a stainless steel. Samples were also produced with a thin, high purity ($\geq 99.95\%$) nickel foil serving as an interlayer between the low-alloyed steel and the aluminium in order to prevent formation of iron-aluminides at the interface. The steel types had chemical compositions as listed in Table 4. Mechanical properties of the steels and aluminium are listed in Table 5.

The stainless steel, referred to as 316, was a $316L$-type stainless steel. 316-steel samples were received as sheets measuring $30 \times 120 \times 1mm$, and cut in half using a Struers Labotom-5 stationary disc cutter. The resulting dimension was $15 \times 120 \times 1mm$. The low-alloyed steel, referred to as 355, was a *SSAB DOMEX 355 MC E* steel and was received as a plate measuring $5mm$ in thickness. The 355-steel was thus rolled down to a thickness of approximate $1mm$ prior to roll-bonding, in order to neglect the effect of thickness in the experiments to come. Due to the unfortunate work-hardening this led to, the 355-steel was recovered and recrystallised at $750°C$ for $4hours$ in Ar-atmosphere, before being quenched in room-tempered water. This heat-treatment served to revert the mechanical properties back to initial state. Samples measuring $15 \times 120 \times 1mm$ were cut from steel, also by the stationary disc cutter. The aluminium was received as a rolled sheet measuring $0.40mm$ in thickness. Samples measuring $15 \times 120 \times 0.4mm$ were cut with a sharp steel-made scissor. The nickel thin foil measured $0.1mm$ in thickness, and samples measuring $15 \times 120 \times 0.1mm$ were cut with a scissor.

Table 4: Chemical composition of the 355 and 316 steels $[wt\%]$. C_{eq} is the carbon equivalent.

	Fe	C	Al	Si	Ni	Mn	Nb	Cr	Mo	C_{eq}
355	Bal.	0.069	0.046	0.01	0.03	0.62	0.023	-	-	0.18
316	Bal.	0.022	-	0.336	10.060	1.298	-	16.645	2.025	-

Table 5: Mechanical properties of the metals as in pre-rolled state. Values for 355-steel are obtained after initial thickness reduction and heat treatment.

	Yield strength $[MPa]$	Ultimate tensile strength $[MPa]$	Vickers hardness $[HV]$
355	174	450	98
316	315	611	151
AA1080	113	120	36

3.2 Overview of experimental procedures and samples produced

Table 6 shows an overview of all samples produced in this report. Different series can be separated by steel type, brushing direction and use of interlayer, and notations are given thereafter.

Table 6: Overview of all samples prepared. Samples can be classified after steel type, brushing direction and use of interlayer. *Sample $355Ni_5$ was chosen for intermetallic layer growing.

Sample ID	Steel	Interlayer	Brushing direction
RD_1	355	No interlayer	RD
RD_2			
RD_3			
RD_4			
RD_5			
355_1			TD
355_2			
355_3			
355_4			
355_5			
316_1	316		
316_2			
316_3			
316_4			
316_5			
316_6			
316_7			
$355Ni_1$	355	Nickel	
$355Ni_2$			
$355Ni_3$			
$355Ni_4$			
$355Ni_5$*			

Samples were produced and roll-bonded according procedures presented in Figure 8. Sample $355Ni_5$ was selected for heat-treatment and intermetallic layer growth, as can be read from the flow chart.

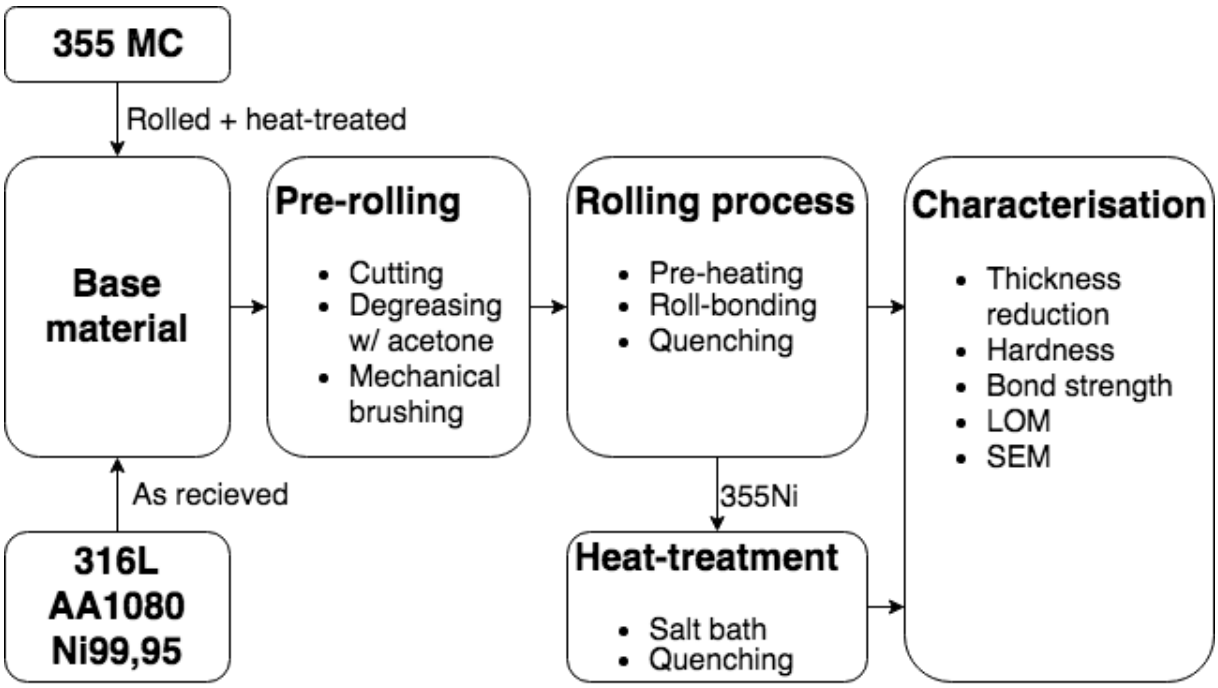

Figure 8: Experimental procedures flow chart. Only the 355-steel was processed prior to the roll-bonding procedure. Sample $355Ni_5$ was chosen for heat-treatment and intermetallic layer growth.

The following sections describe the experimental procedures and characterisation methods in detail.

3.3 The roll-bonding process

The steel and aluminium sheets were rolled together in a two high rolling mill in one single step. In order to keep the sheets in position during rolling they were fastened with two rivets, one on each end. The steel was chosen for the top and bottom sheets with the aluminium in centre. See Figure 9 for an illustration of the stacking order. This stacking order made peel-testing easier, and also prevented the aluminium from sticking to the rollers.

For the samples prepared with metallic interlayer, a $0,1mm$ thick nickel foil was placed between aluminium and one steel sheet.

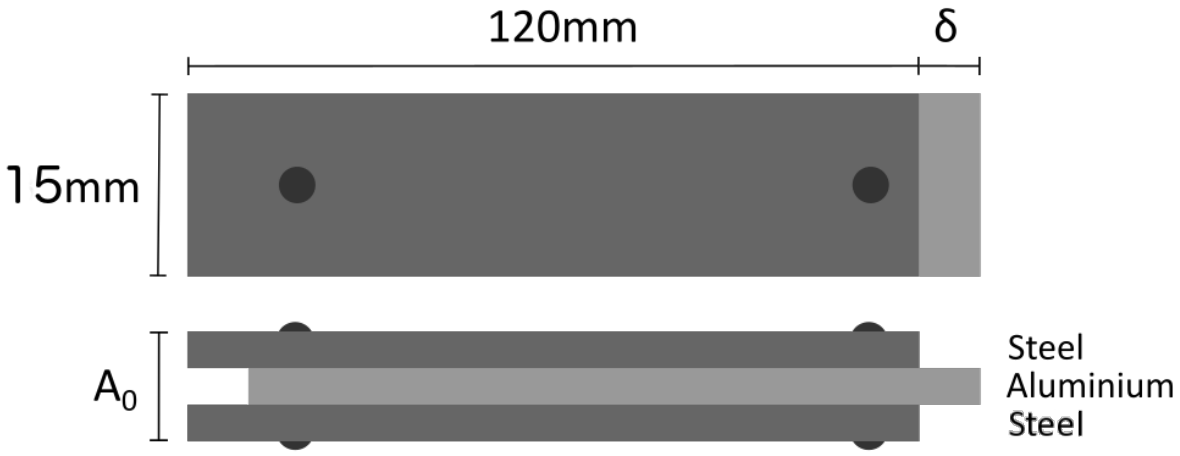

Figure 9: Top and side view illustrations of the three-layer samples pre rolling. The steel and aluminium sheets are offset by a small distance $\delta \approx 10mm$ in order for the rollers to get a better grip. The rivets are indicated with a dark colour. Initial dimensions are $15mm \times 120mm$ and a total thickness A_0. Sketch made by the author.

The rollers each had diameters of $205mm$ and adjustable rolling speed. Roll-bonding was conducted with the speed set to Level 3, which corresponds to a rolled product pace of $106mm/sec$.

Table 7: Speed on roll-mill

Level	Measured rolling frequency $[sec^{-1}]$	Calculated pace $[\frac{mm}{sec}]$
3	0.16505	106.3

3.3.1 The pre-rolling procedure

First, specimens were cut in the desired dimensions and holes for rivets were introduced with a manual drilling machine. Dimensions chosen for the experiments were $120mm \times 15mm$ with the thickness depending on the individual sheet/plate. A disc cutter was used to cut the steels while a scissor was chosen to cut aluminium and nickel.

Secondly, the specimens were cleansed chemically and mechanically. The surfaces target for bonding were scrubbed with acetone to remove grease and dirt. This procedure was conducted by squirting acetone onto a paper towel and scrubbing the specimens by hand. The duration of scrubbing was estimated to be about half of a minute on each side. After chemical de-greasing, the samples were mounted on a work-bench with a clamp for mechanically removal of the oxide layer and work-hardening of the surface. A $0.3mm$ rotating steel-wire-brush mounted on an electrical hand-held grinder was used to give the surfaces desired finish. Brushing was conducted in one single go in a steady state speed. One operator held the grinder/brusher while another operator directed the path of movement and steered the brushing. Brushing was conducted in the transverse direction (TD) except for the pre-study. The nickel interlayer was not brushed.

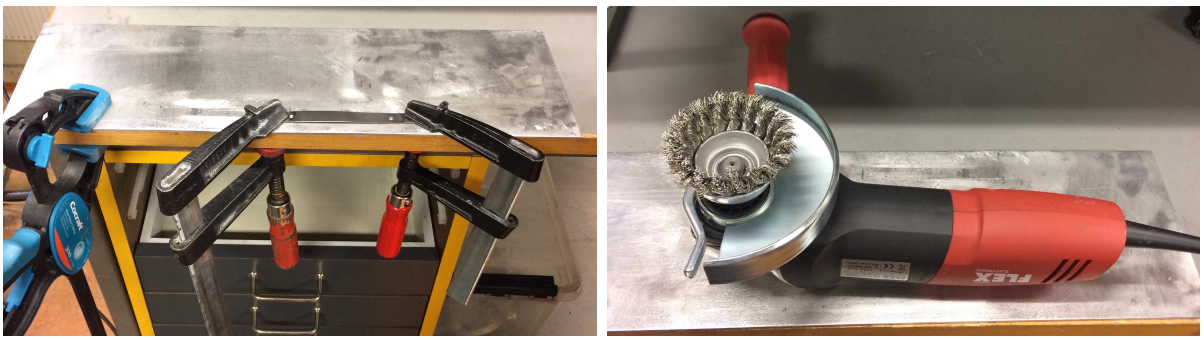

(a) **(b)**

Figure 10: **(a)** The work-bench for brushing procedure with a sample fastened with clamps. **(b)** The $0.3mm$ rotating steel-wire-brush mounted on the hand-held grinder.

After brushing, the specimen were cleansed with compressed air to remove any debris left from the brushing procedure. Finally the sheets were stacked in the correct order and the rivets were fastened.

3.3.2 Roll-bonding

To soften the steels and reduce the flow stresses, all specimens were rolled at an elevated temperature estimated to be 150°C. This estimation was based on previous testing conducted by Solhaug [39], where he found that heating a three-layer sandwich-component of steel and aluminium in 185°C air for 10 minutes would result in core temperature being approx 150°C. All samples were thus heated prior to roll-bonding. From the samples were extracted from the furnace to being fed into the rollers, it took approximate $3-5seconds$.

Post rolling, the samples were immediately immersed in cold water before thickness values were measured with a caliper. Samples for peel-testing and hardness-testing were cut from each specimen at a stationary disc cutter.

3.4 Heat treatments for growing intermetallic layers

Sample $355Ni_5$ was chosen for growth of intermetallic layers. The specimen was cut in eight smaller pieces measuring $\approx 15mm$ in width. The eight samples were heat-treated in salt baths on temperatures and times as given in Table 8. One series was made with constant $T = 450°C$ and times ranging from $1min$ to $1hour$, and one series was made with constant holding time $t = 60min$ and temperatures ranging from $400 - 550°C$.

Table 8: Overview of heat-treated samples $355Ni_5$.

		Immersed time $[minutes]$				
		1	4	15	34	60
Temperature $[°C]$	550					X
	500					X
	450	X	X	X	X	X
	400					X

3.5 Mechanical testing

From the heat-treated samples, smaller pieces were cut to examine hardness, total thickness, chemical composition across the interface and visual inspection. The surface of interest was the one perpendicular to rolling direction and perpendicular to the steel-aluminium interface, namely the RD-ND plane. Figure 11 shows an illustration of the samples post-rolling, with dashed lines indicating the cuts made. Chequered pattern shows the surface/plane of interest. Small pieces of approx $15mm$ length and $10mm$ height were cut on a stationary disc cutter and cast in an EpoFix^{TM} mould to ease the polishing.

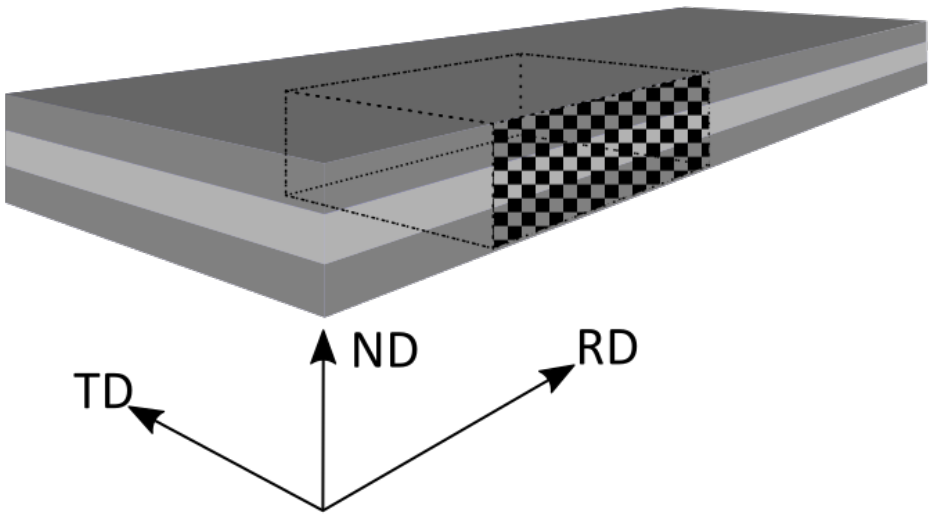

Figure 11: Illustration of the cuts made on the samples. Area of interest is highlighted with a chequered pattern, and directions are indicated with arrows. RD is rolling direction, ND is normal direction and TD is transverse direction. Area of interest is located in the RD-ND plane. Sketch made by the author.

3.5.1 Tensile strength

Samples for tensile testing was cut from the base material, i.e. the 355-steel plate and $AA1080$ roll. As mechanical properties was known for the 316-steel in as-received conditions, it was not further tested. Dimensions for the test specimen was set to $100mm \times 12mm$ with a reduced section measuring $8mm$ in width. Thickness for the specimen was equal that of the base material, i.e. $0.9mm$ and $0.4mm$ for steel and aluminium respectively. Machining of the specimen was carried out by professional mechanical engineers working at campus.

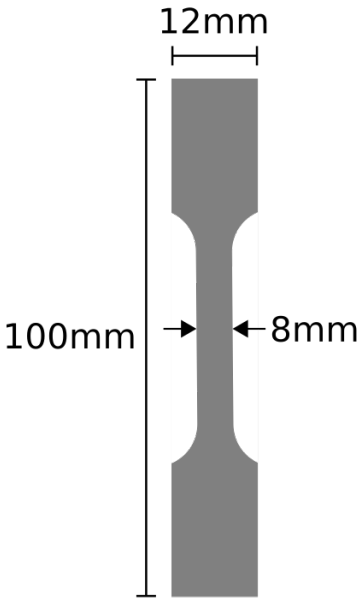

Figure 12: Illustration of the tensile test specimen with dimensions displayed. Note that thickness of the specimen are not displayed as it might vary. Sketch made by the author.

Testing was conducted on a MTS 810 Material Testing System with 25mm extensiometer applied.

3.5.2 Peel-strength

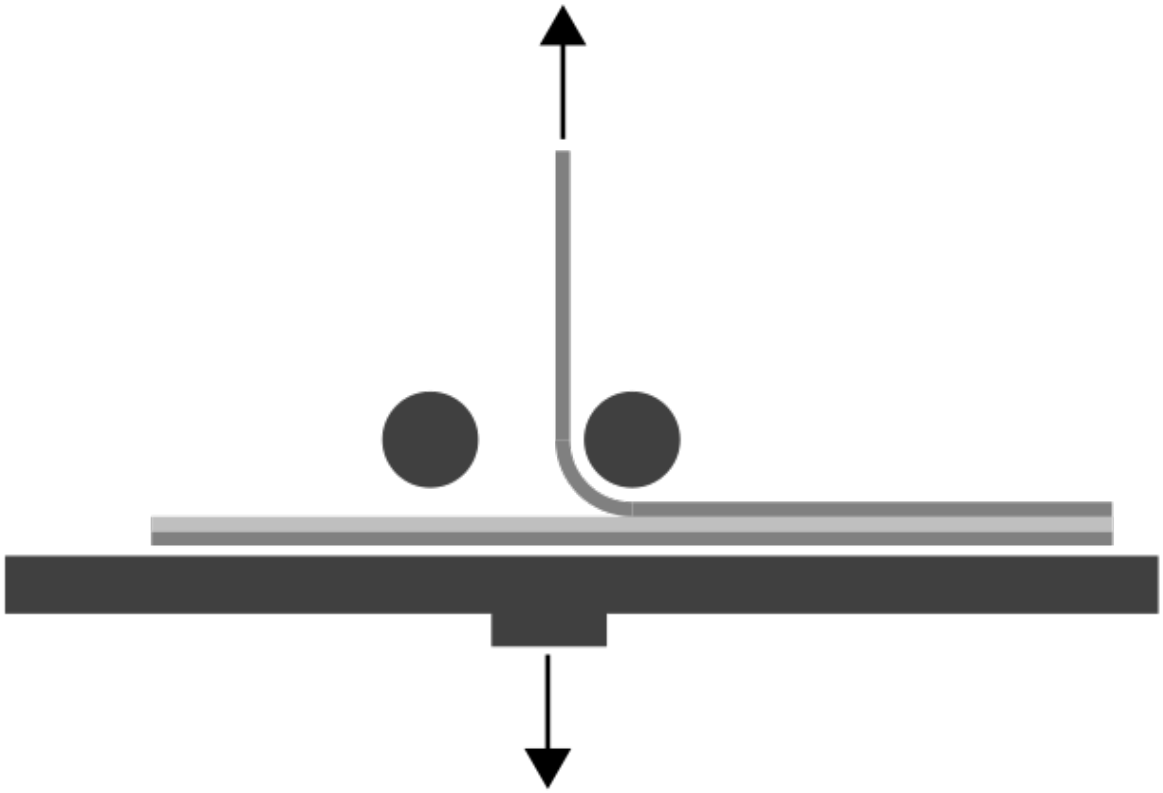

Figure 13: Cross-sectional illustration of the peel-test-rig with rollers, all coloured dark grey. The three-layer sample is illustrated in brighter shades of grey. The uppermost steel-layer is being pulled perpendicular to the steel-aluminium-interface plane. Arrows indicate direction of the force applied. Designed by Solhaug [39]. Sketch made by the author.

Bond strength was tested by conducting a modified ASTM D3167 test [37], similar as the test conducted by Wu *et al.* [40] on his steel-aluminium roll-bonded samles. Roll-bonded samples were cut in pieces measuring $1cm$ in width by a water-jet cutter. The samples were opened in one end so that the different steel layers were separated before being fed into the rig illustrated in Figure 13. One of the steel layers was bent upwards and attached to the tensile machine while the other end was free to slide. The sample was held in place by rollers. Tensile force was applied to the set-up leading to a controlled peel of the two steel layers. Applied force was recorded and used for bond strength calculations by Equation 11.

3.5.3 Hardness

Hardness testing was conducted after LOM analysis with no further sample treatment. Hardness testing was conducted on a Zwick Roell Indentec Vickers hardness tester. $0.1kg$ load was chosen for the aluminium, $5kg$ load was chosen for the 355-steel and $10kg$ load for the 316-steel. Holding time was set to $10sec$. Five indentations were made per metallic layer per sample in order to obtain an average value and standard deviation.

3.6 Characterisation

3.6.1 Light Optical Microscopy

The moulded samples were ground by standard metallurgical methods prior to analysis in LOM. SiC paper with roughness values of 500-800-1200-2400, 3 and $1\mu m$ diamond paste polishing and finally vibratory polishing for $17hours$ gave the desired finish. Thickness measurements were conducted on $10X$ magnification on a Leica MeF4 inverted microscope with a measuring tool embedded in the microscope software. The software allowed for lines to be drew across the area of interest, and it automatically calculated the length of the line. Five measurements were made per value obtained.

3.6.2 Scanning Electron Microscopy

To avoid electrical charging in SEM, samples were removed from the mould after LOM imaging. This was obtained by placing the samples in a vice and forcing the mould to crack open, separating the samples from the non-conductive mould.

The SEM applied was a Zeiss Ultra 55 Field Emission SEM equipped with an Everhart-Thornley secondary electron detector and a Bruker QUANTAX EDS detector. An accelerating voltage of $15kV$, "low current mode" and aperture size of $30\mu m$ was applied.

Selected fractured surfaces from peel-testing was analysed with secondary electrons imaging and EDS area scan. Cross-sections from heat-treated samples were analysed with secondary electrons and EDS line scan in order to detect any intermetallic phases present.

4 Results

This chapter presents the results in a hierarchic manner. First, an investigation of the effect of brushing direction is presented, before the results of the main study are presented in sections depending on metal combinations. Each of the sections are further divided into mechanical testing results and characterisation.

All except two samples were successfully roll-bonded. Samples RD_1 and RD_2 failed in the meaning of sideways sliding during rolling and were thus excluded from further procedures/investigations. Samples $RD_{3\rightarrow5}$ and $355_{1\rightarrow5}$ were, in addition to being a part of the main study, also used for a pre-study of the effect of brushing direction. Result from this pre-study laid guidance on how the other samples were brushed.

Prestudy: Investigation of the effect of brushing direction

Figure 14 shows peel strength as function of steel deformation. Samples brushed in TD are plotted as circles whereas samples brushed in RD are plotted as stars. Standard deviations are displayed as error bars. All peel-strengths are in the range from $5-13\frac{N}{mm}$, and steel deformations are in the range from $52-64\%$. Samples brushed in TD have in general higher peel strengths and larger deviation of the data. Values of RD-samples fall within the errorbars of those brushed in TD.

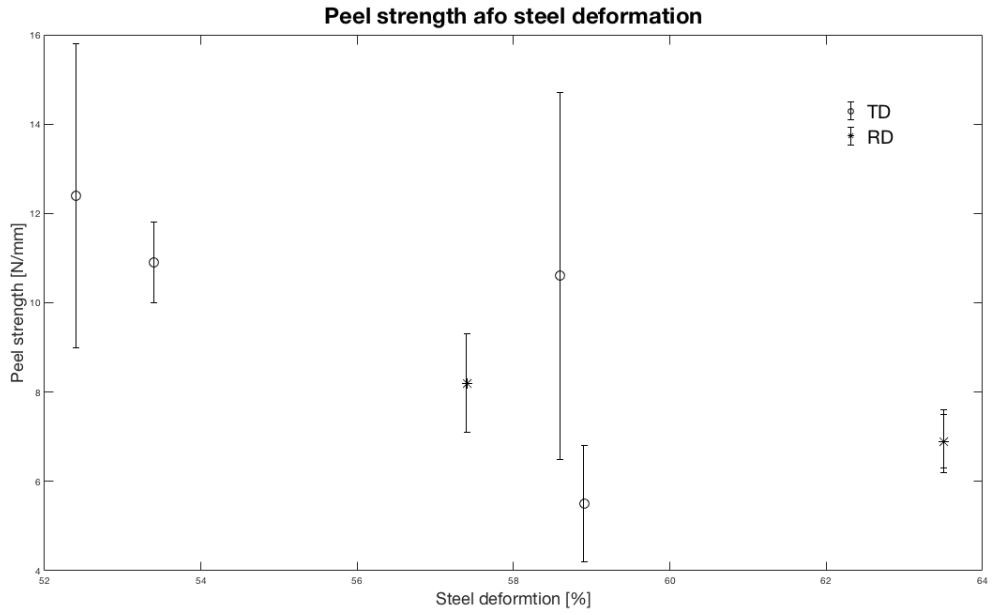

Figure 14: Peel strength in rolling vs. transverse direction. Transverse direction peel results are plotted as circles, rolling direction peel results as stars. Error bars represent standard deviation of test results. Values are obtained by taking average value over an area of interest. All average values were calculated by starting $40mm$ from start of the test and ending approximate $20mm$ before the test ended.

Figure 15 shows LOM images of the brushed surfaces of 355-samples, both brushing in RD

and TD. Images reveal high topographic differences and a repeating pattern of plastically deformed material on the surfaces. Surfaces look similar, only the orientation vary.

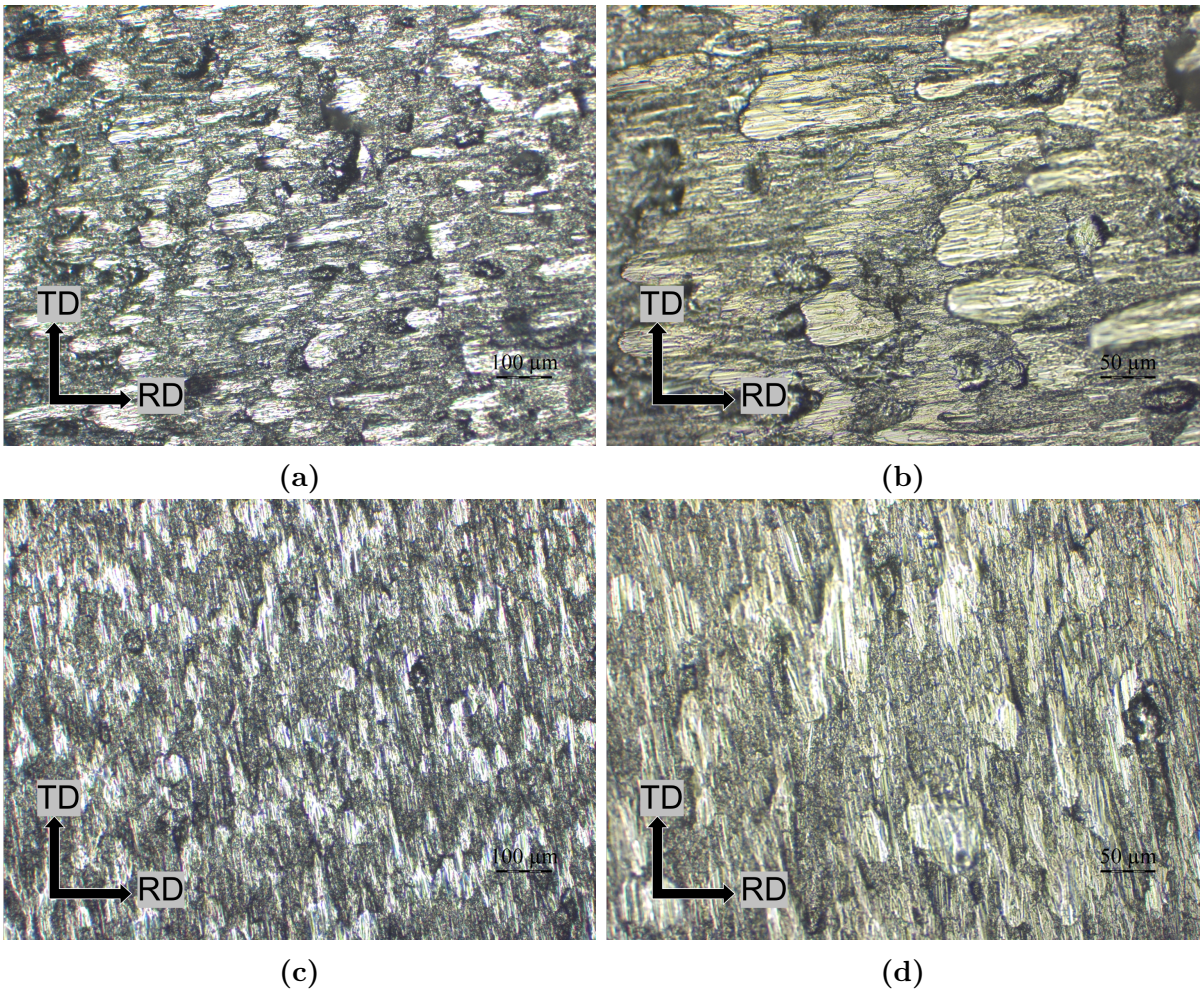

Figure 15: LOM images showing the brushed surfaces on a sample of 355 MC steel. **(a)** Brushing in RD at 10X magnification. **(b)** Brushing in RD at 20X magnification. **(c)** Brushing in TD at 10 magnification. **(d)** Brushing in TD at 20X magnification.

4.1 Roll bonding of AA1080 and 355

4.1.1 Mechanical testing

Laminated samples were produced exclusively to test hardness of the aluminium after the pre-rolling heating at $185°C$. The result showed that the hardness of aluminium stacked between 355-sheets was reduced to $31HV$ (from initially $36HV$, see Table 5), which is a result of static recovery.

Table 9 shows all mechanical testing results for samples $RD_{3\to5}$ and $355_{1\to5}$. Reduction values are calculated by Equation 10 from measurements taken at cross-sectional images taken in LOM. Aluminium have for all samples experienced more plastic deformation than steel. Hardness measurements show that the steel have hardened to approximate $200 - 230HV$ (from initially 98, see Table 5) whereas aluminium have experienced net recovery to a hardness of approximate $20 - 30HV$ (form initially $36HV$, see Table 5). Peel strengths vary from $5,5$ to $12,3\frac{N}{mm}$.

Table 9: Thickness reduction, hardness and peel strength. Thickness reduction values are calculated with Equation 10. Note the artificial high value for aluminium hardness on sample 355_3. Smaples RD_5 and 355_1 failed at peel testing and have no value for peel strength.

Sample ID	Reduction [%]			Hardness [HV]		Peel strength
	Steel	Aluminium	Total	Steel	Aluminium	$[\frac{N}{mm}]$
RD_3	64	69	64	207	22	6,9
RD_4	57	76	60	200	22	8,2
RD_5	58	74	61	200	18	-
355_1	56	61	57	216	25	-
355_2	59	73	61	211	26	10,6
355_3	59	72	61	237	49	5,5
355_4	53	62	55	230	28	10,9
355_5	52	70	55	229	19	12,3

4.1.2 Fractography and EDS scans

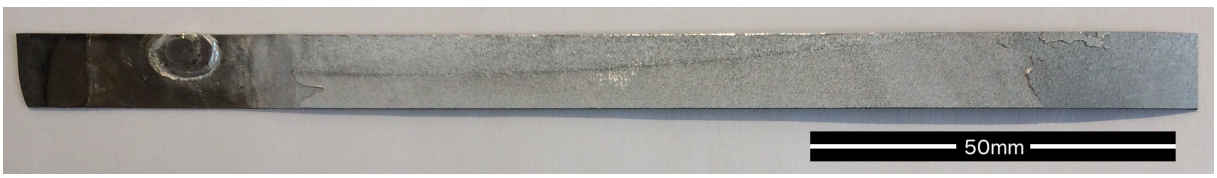

Figure 16: Sample 355_3 after peel-testing. Crack was initiated at left hand side of the sample (where the rivet can be seen) and propagated towards right as the sample was peeled.

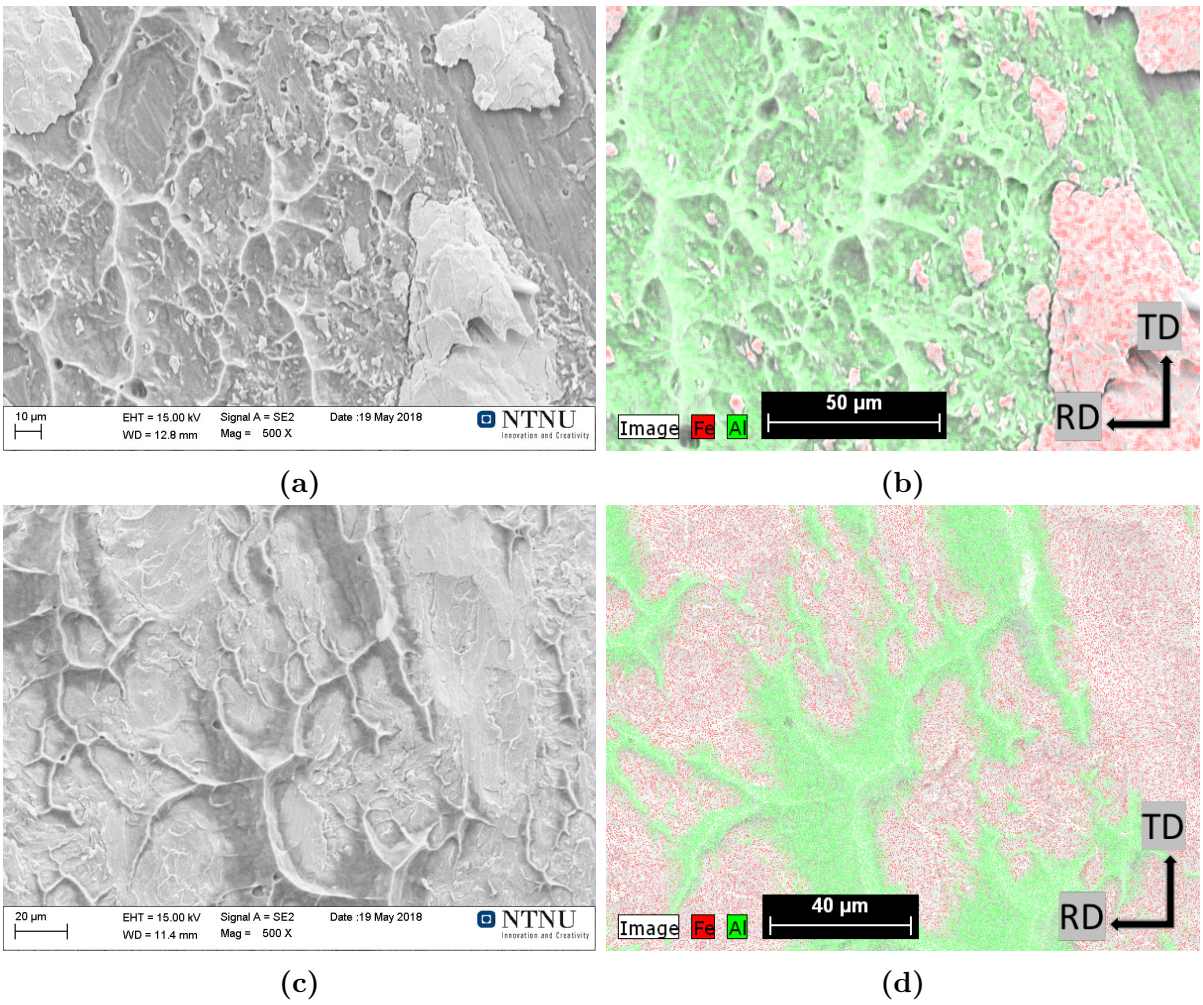

Figure 17: SEM images and EDS scans of fracture surfaces on sample 355_5. **(a)** Aluminium surface. **(b)** EDS scan of the aluminium with residual iron coloured red. **(c)** Steel surface. **(d)** EDS scan of the steel surface with residual aluminium coloured green.

Figures 16 and 17 show fractography of sample 355 on a macroscopic and microscopic level respectively. On a macroscopic level one can see the crack propagation between steel and aluminium, whereas residual metal pieces can be seen on a microscopic level. EDS scans show residual steel (red) on the aluminium surface (green) and vice versa.

Dimples can be seen on the fractured aluminium on both sides (aluminium and steel side). The residual steel pieces on the other hand have flat fracture surfaces with distinct steps like in a stairway. No dimples are visible on the steel.

4.2 Roll bonding of AA1080 and 316

4.2.1 Mechanical testing

Just as with 355-steel, a laminated sample was also produced exclusively to test the hardness of aluminium after the pre-rolling heating. The result showed an aluminium hardness of $32HV$, which is a decrease from $36HV$ as received. The decrease is a result of static recovery.

Table 10 shows all mechanical testing results for samples $316_{1\rightarrow7}$. Reductions are calculated by Equation 10 by use of measurements taken at cross-sectional images in LOM. All samples have experienced higher degree of deformation in the aluminium layer than in the steel layers, similar to the samples produced with 355-steel. The 316-steel have hardened to approximate $300HV$ whereas the aluminium are approximate equal to as-received state, i.e. $36HV$. Peel strengths vary from 8.4 to 12.2$\frac{N}{mm}$.

Table 10: Thickness reduction, hardness and peel strength for samples $316_{1\rightarrow7}$. Thickness reduction values are calculated with Equation 10. Note how three of the samples failed during peel testing and have not obtained peel strength values.

Sample ID	Reduction [%]			Hardness [HV]		Peel strength
	Steel	Aluminium	Total	Steel	Aluminium	[$\frac{N}{mm}$]
316_1	34	41	35	297	32	8,4
316_2	37	52	39	303	33	11,1
316_3	35	54	38	302	34	-
316_4	37	59	41	297	35	4,6
316_5	33	50	36	293	36	-
316_6	46	54	48	312	40	12,2
316_7	45	50	46	210	32	-

4.2.2 Fractography and EDS scans

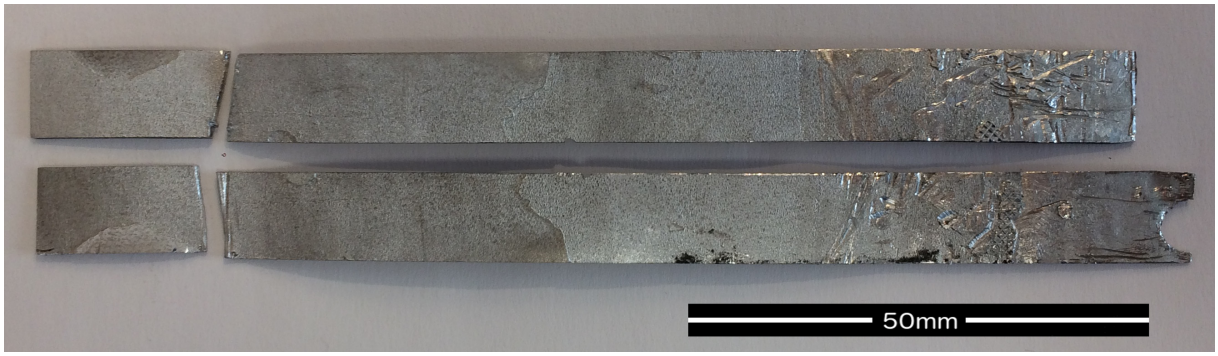

Figure 18: Sample 316_4 after peel-testing. On the left hand side the pieces cut for SEM can be seen. Marks after the tensile machine can be seen on the right hand side. Pay attention to how the fracture changed side about halfway through (centre of specimen) and cut through the aluminium layer.

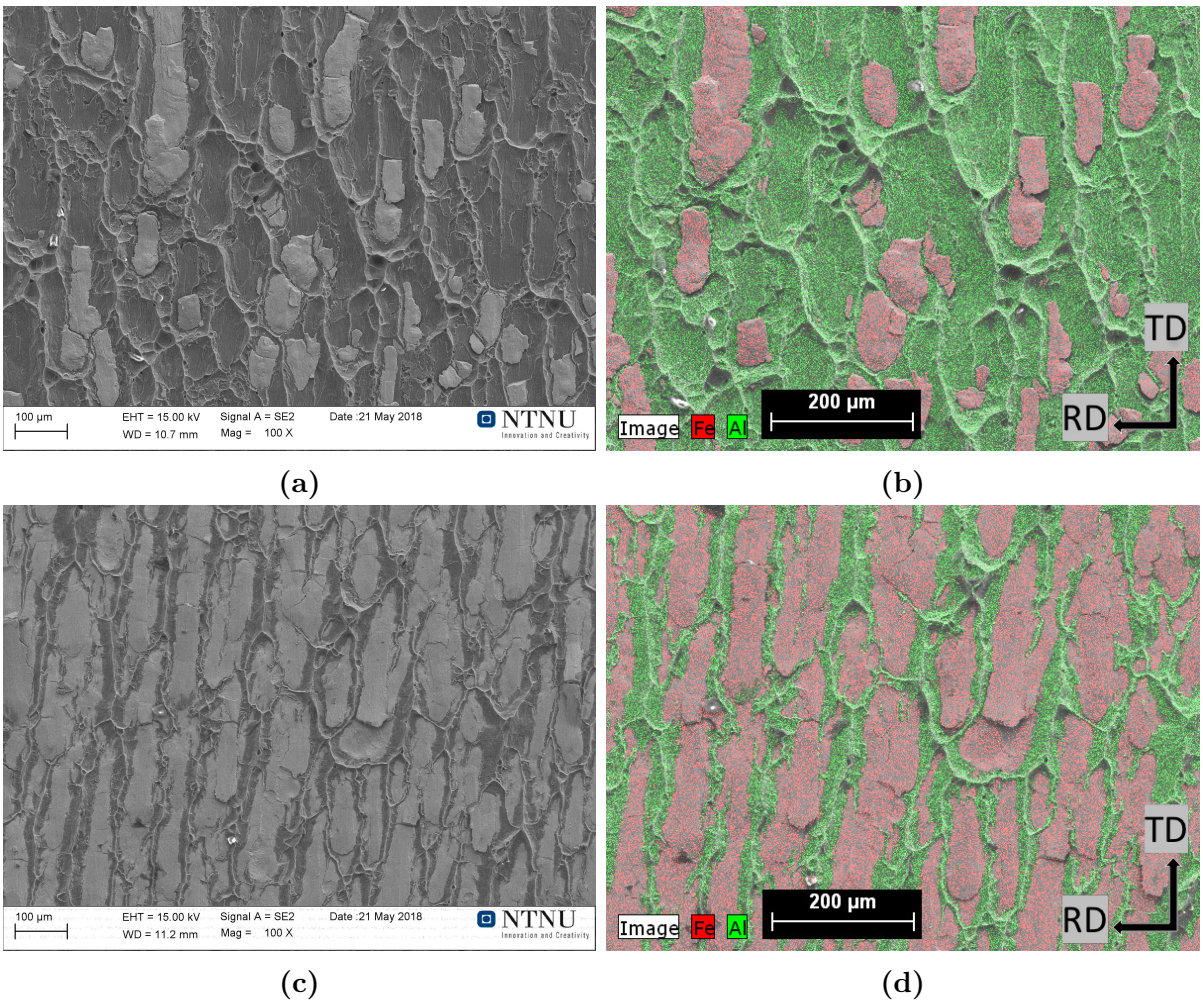

Figure 19: SEM images and EDS scans of fracture surfaces on sample 316_4. **(a)** Aluminium surface. **(b)** EDS scan of the aluminium with residual iron coloured red. **(c)** Steel surface. **(d)** EDS scan of the steel surface with residual aluminium coloured green.

Figures 18 and 19 show fractography of sample 316 on a macroscopic and microscopic level respectively. On a macroscopic level the crack propagation can be seen between steel and aluminium, changing interface about halfway and cutting through the aluminium. Microscopic images show residual metal pieces on the fractured surfaces. EDS scans show residual steel (red) on the aluminium surface (green) and vice versa.

The fractured aluminium on both sides (steel and aluminium side) have formed dimples, whereas no dimples can be seen on the fractured steel surfaces. Residual steel pieces on the aluminium surface are longer in TD than in RD. The residual aluminium have formed what looks like "hill-sides" directed in TD.

4.3 Roll bonding of AA1080 and 355 with Ni-interlayer

4.3.1 Mechanical testing

Table 11 shows all mechanical testing results for samples $355Ni_{1\rightarrow5}$. Just as for the two previous series (355- and 316-series), aluminium have experienced more deformation than the steel. The total degree of deformation is in general high, approximate 60%. The steel sheets have hardened to approximate $200HV$ whereas the aluminium have softened to approximate $25-30HV$. Peel strengths are generally poor, $2-3\frac{N}{mm}$. Mechanical testing was not conducted on the interlayer.

Table 11: Thickness reductions, hardness measurements and peel strengths of samples $355Ni_{1\rightarrow5}$. Thickness reduction values are calculated with Equation 10. Note that sample $355Ni_1$ failed during peel testing. *Sample $355Ni_5$ was chosen for intermetallic layer growth and thus not peel-tested.

Sample ID	Reduction [%]			Hardness [HV]		Peel strength
	Steel	Aluminium	Total	Steel	Aluminium	[$\frac{N}{mm}$]
$355Ni_1$	62	66	63	201	31	-
$355Ni_2$	59	68	60	192	32	2,1
$355Ni_3$	60	69	61	206	28	2,3
$355Ni_4$	63	67	63	198	25	3,1
$355Ni_5$*	62	64	61	187	22	Not tested

4.3.2 Fractography and EDS scans

Figures 20 and 21 show macroscopic and microscopic fractography, respectively. On a macroscopic level the crack propagation can be seen between nickel and steel, leaving close to pure metal surfaces. On a microscopic level the nickel surface shows marks/indentations, and at some points also foreign pieces attached. The steel surface on the other hand has several particles which size match those from the indentations on the nickel face. EDS scans reveal small amounts of residual metal pieces on the fractured surfaces. Residual steel (green) and residual aluminium (blue) can be seen on the nickel surface (red). Steel is concentrated at certain distinct sites at the nickel face; at the foreign particles and in some indentations. Residual nickel (red) and aluminium (blue) can be seen on the steel surface (green). Nickel is concentrated at the particles on the steel surface, but the overall concentration is low. EDS scans indicate small amounts of aluminium at certain concentrated sites.

Figure 20: Sample $355Ni_3$ after peel-testing. Crack propagated from right hand side (where the rivet can be seen) towards left.

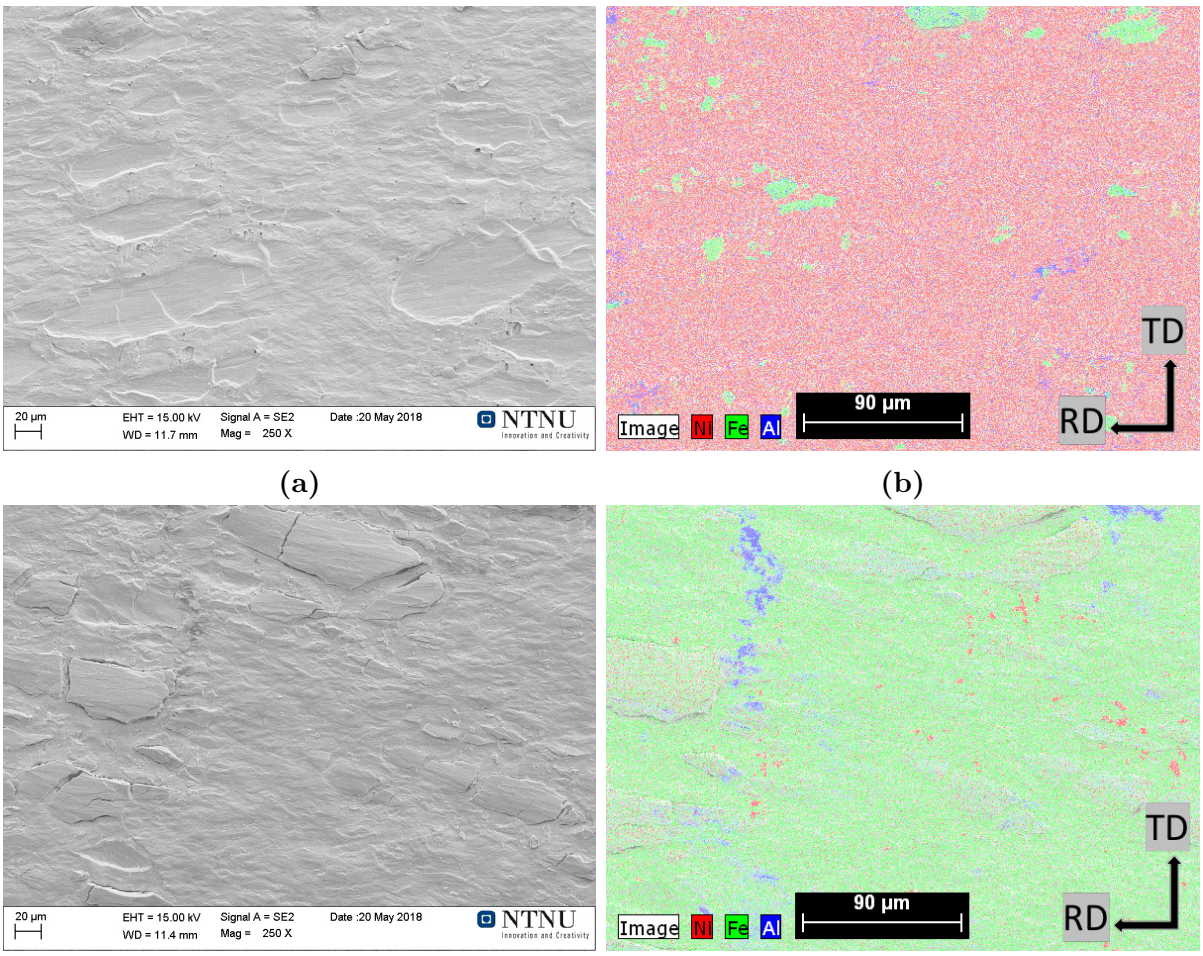

Figure 21: SEM images and EDS scans of fracture surfaces on sample $355Ni_3$. **(a)** Nickel surface. **(b)** EDS scan of the nickel surface with residual iron and aluminium coloured green and blue respectively. **(c)** Steel surface. **(d)** EDS scan of the steel surface with residual nickel and aluminium coloured red and blue respectively.

4.3.3 Characterisation of intermetallics in LOM

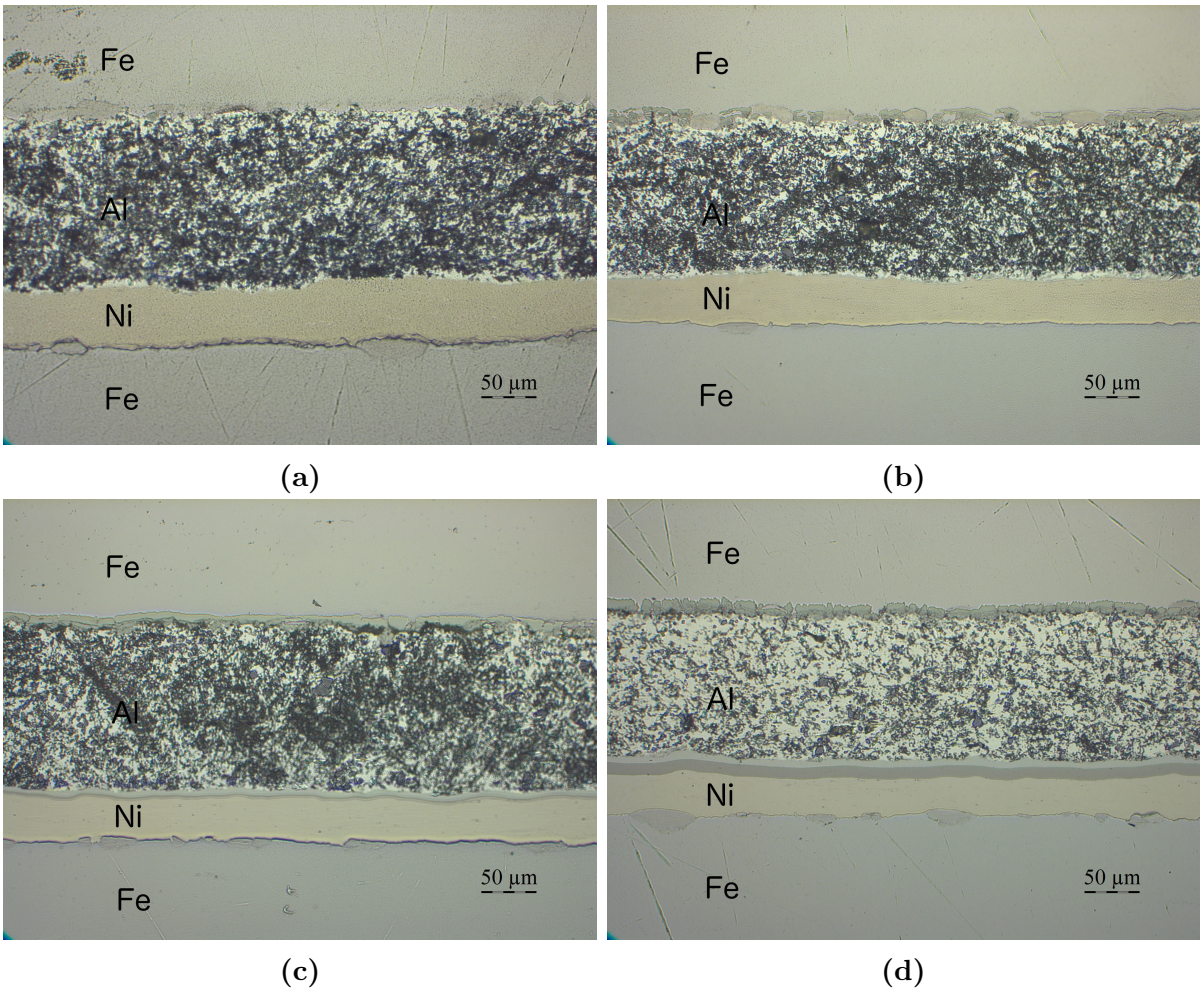

Figure 22: Lom images showing stacking and reaction layers post heat-treatment for 1 hour at **(a)** 400°C, **(b)** 450°C, **(c)** 500°C and **(d)** 550°C. While no reaction layers between aluminium and nickel can be observed at temperatures below 500°C, a discrete reaction layer can be seen between steel and aluminium for all temperatures investigated.

Figure 22 shows cross-sectional images of sample $355Ni_5$ heat-treated for $1hour$. The dark colour in the aluminium layer is due to unintentional etching during an automatic polishing process, using a basic polishing fluid. The steel-aluminium reaction layers are discrete and with uneven thicknesses, whereas aluminium-nickel reaction layers are even and continuously. At samples heat-treated at 500 and 550°C, two distinct layers can be seen on the nickel-aluminium interface.

Cracks can clearly be seen at the steel-nickel interfaces, along with discreetly distributed particles.

4.3.4 Characterisation of intermetallics in SEM

In SEM, intermetallics that could not be detected in LOM was observed. EDS scans were taken across interfaces and over intermetallic phases in order to gain a deeper understand-

ing of the phases formed. Average intermetallic layer thickness values are presented in Table 12. For the sample immersed for $1minute$, no intermetallic layer could be detected. Intermetallics tend to increase in thickness with increasing time and/or temperature, with some values off. No intermetallic was observed at the steel-nickel interfaces.

Table 12: Intermetallic layer thickness, Fe-Al/Al-Ni-interface [μm]. Samples heated at 500 and $550°C$ grew two distinct layers and individual thicknesses are displayed in parenthesis, the one adjacent to aluminium first.

		Immersed time [$minutes$]				
		1	4	15	34	60
Temperature [$°C$]	550					5,9/16,1(6,7+9,4)
	500					6,8/6,4(3,0+3,4)
	450	-/-	2,4/0,5	3,3/1,1	6,2/1,9	3,1/1,8
	400					0,6/0,3

Figure 23 shows a cross-sectional overview image of sample heated at $550°C$ for $1hour$. The steel-nickel interface is characterised by cracks and particles, and no visible intermetallic phase. Closer inspections and EDS scan across the interface (Figure 24) supports the initial observations, with the EDS scan showing a distinct boundary between the two metals.

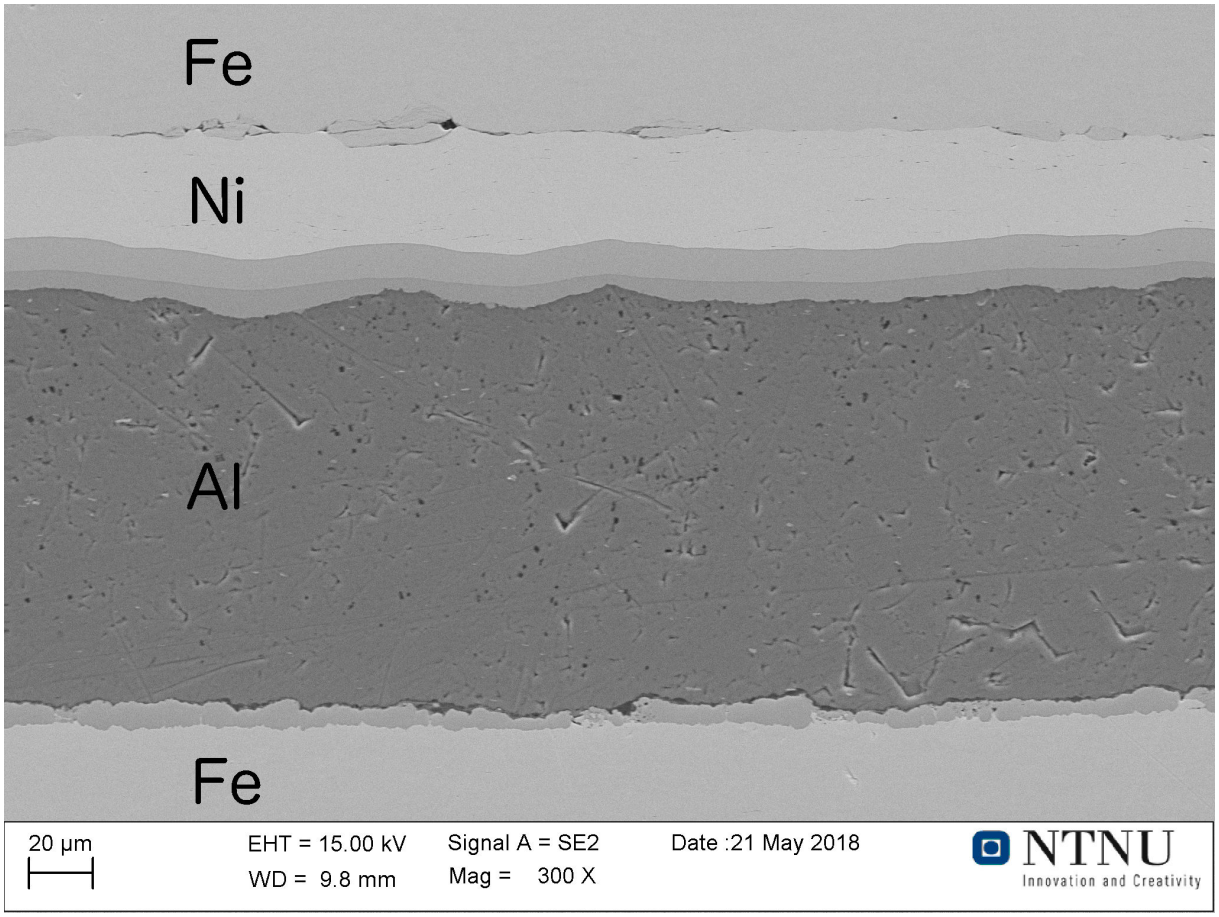

Figure 23: SEM cross-sectional overview image of sample heat-treated for $1hour$ at $550°C$.

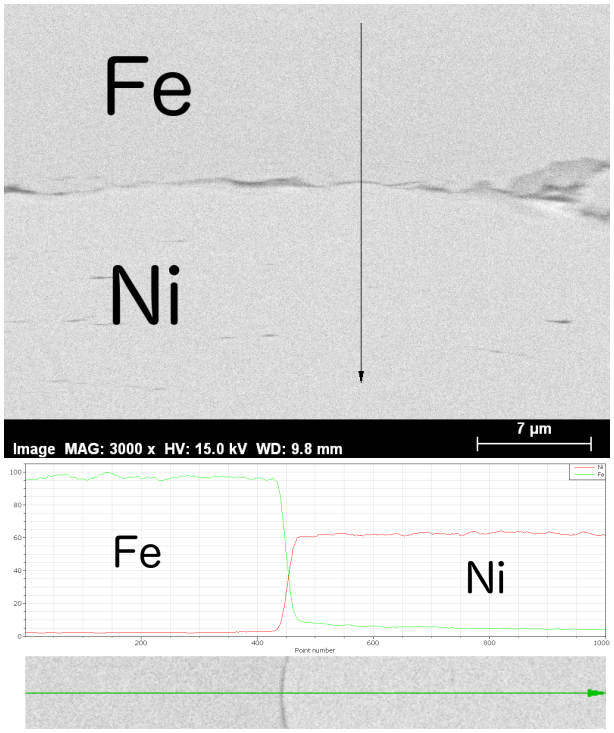

Figure 24: EDS line scan across Fe-Ni interface of sample heat-treated at $550°C$ for $1hour$.

The nickel-aluminium interface (Figure 25) on the other hand shows two intermetallic phases and no cracks. EDS scan across the interface shows gradually decreasing element concentrations in a stepwise manner. The scan shows a high bromine (Br, Z=35) content where aluminium is present. It is certain that the EDS software misinterpret the aluminium signal to be bromine due to its close-to-equal X-ray energies. $Al - K_\alpha$ and $Br - L_\alpha$ radiations have values $1.486keV$ and $1.481keV$ [41], respectively, and can easily be misinterpret. Thus, bromine is displayed in the EDS scan bu should be read as aluminium.

The steel-aluminium interface displayed in Figure 26 shows one intermetallic phase and cracks running between the intermetallic and the aluminium. Bromine is also included in this EDS scan but should be read as aluminium.

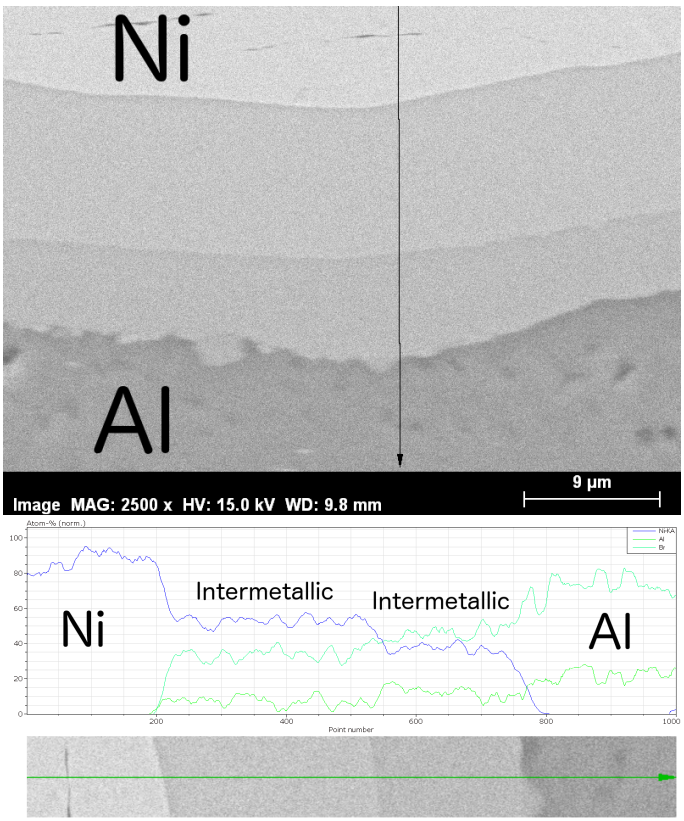

Figure 25: EDS line scan across Al-Ni interface of sample heat-treated at 550°C for 1$hour$.

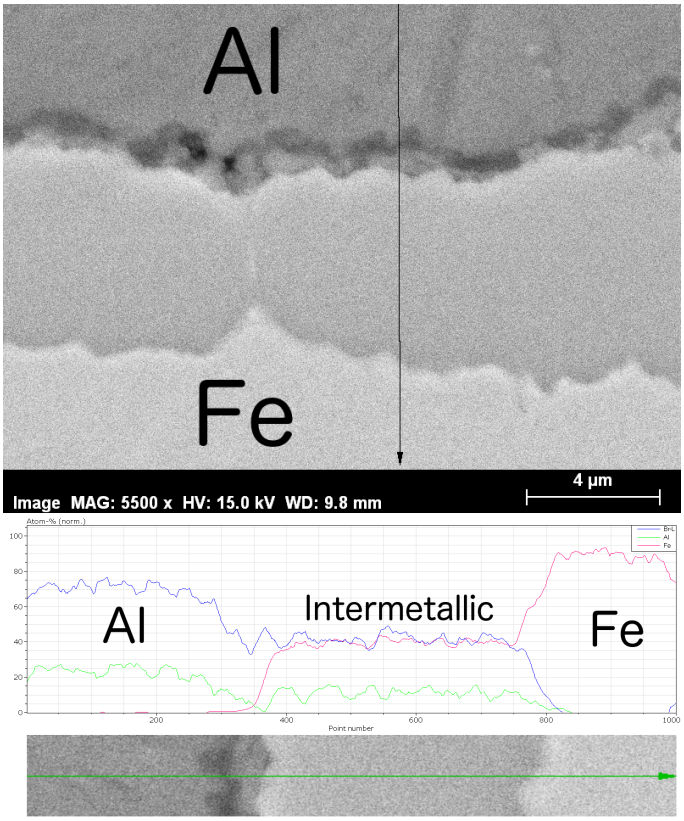

Figure 26: EDS line scan across Al-Fe interface of sample heat-treated at 550°C for 1$hour$.

Figure 27 shows a cross-sectional overview image of sample heated at $500°C$ for $1hour$. The sample is similar to the one heated at $550°C$, with no intermetallic and cracks at the steel-nickel interface, two distinct intermetallics at the aluminium-nickel interface and one intermetallic and cracks at the steel-aluminium interface. The cracks on the steel-aluminium interface are adjacent to the aluminium.

Figure 28 and Figure 29 show closer inspections of steel-aluminium and aluminium-nickel interfaces, respectively. EDS line scan across the steel-aluminium intermetallic show a single phase present. The phase is characterised by an even, steady concentration of steel and aluminium. Bromine is also displayed but should be read as aluminium. On the aluminium side of the intermetallic there is a crack running, whereas the boundary towards steel is irregular. EDS scan across the aluminium-nickel intermetallics show distinct phases with even boundaries.

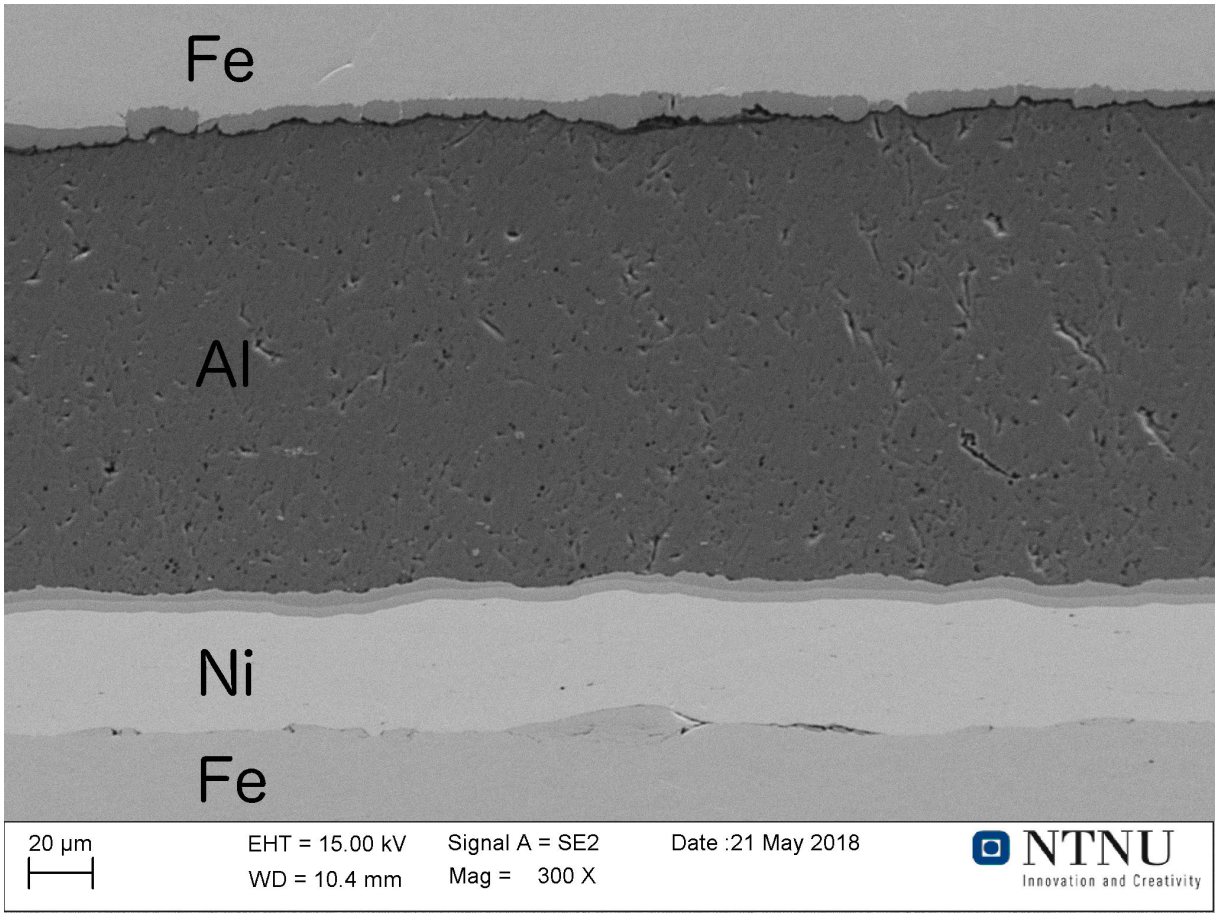

Figure 27: SEM cross-sectional overview image of sample heat-treated at $500°C$ for $1hour$.

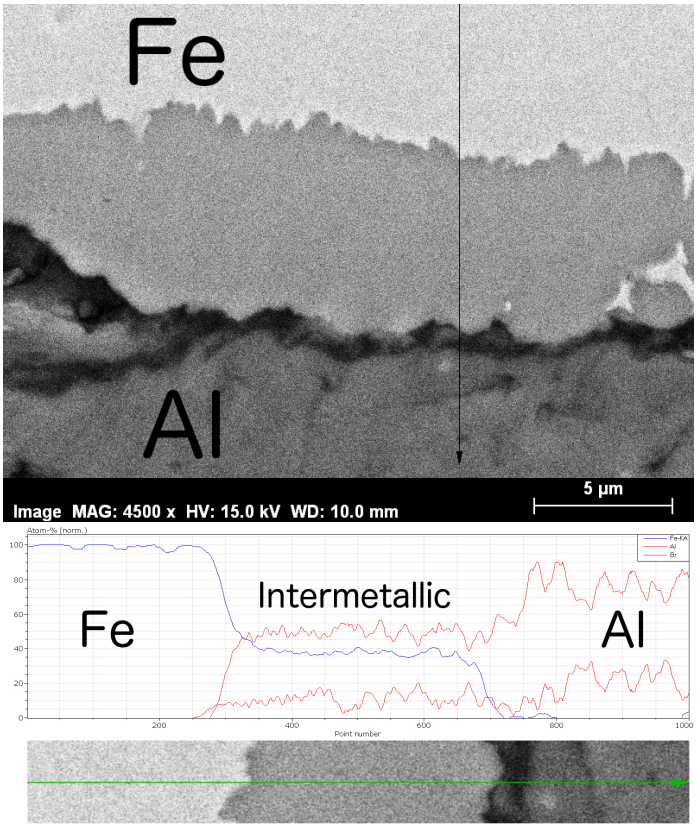

Figure 28: EDS line scan at Fe-Al interface of sample heat-treated at $500°C$ for $1hour$.

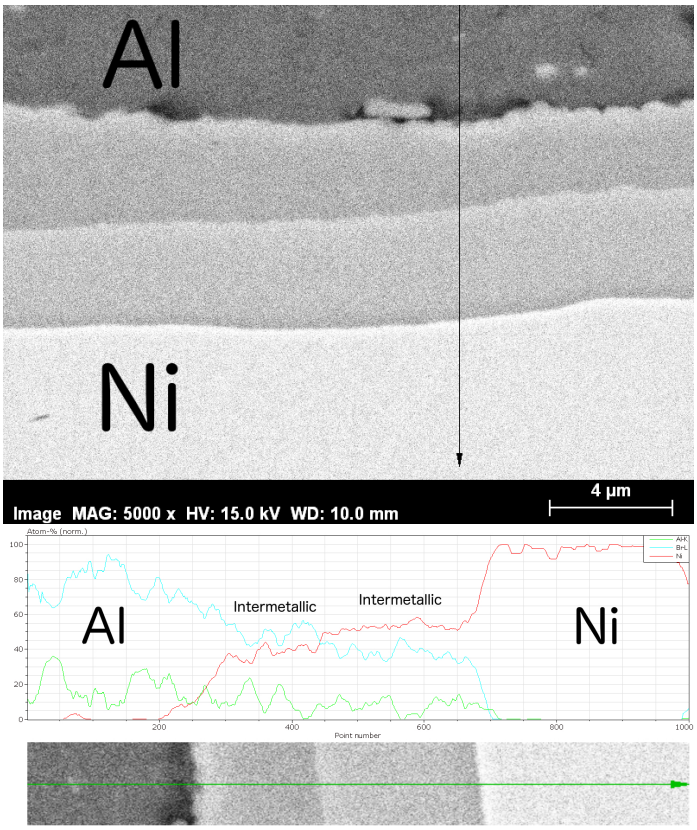

Figure 29: EDS line scan at Al-Ni interface of sample heat-treated at $500°C$ for $1hour$.

Figure 30 shows a cross-sectional overview image of sample heated at $450°C$ for $1hour$. A discrete intermetallic can be seen on the steel-aluminium interface and a continuous intermetallic can be seen on the aluminium-nickel interface. The steel-nickel interface shows no intermetallic, only some particles.

EDS point scans of the particles on the steel-nickel interface reveal they are steel particles, see Figure 31. Figure 32 shows EDS scan across the aluminium-nickel interface, where one phase is present. Figure 33 shows EDS scan across a bulky intermetallic phase on the steel-aluminium interface, at the point where it is thickest. The scan show one single phase.

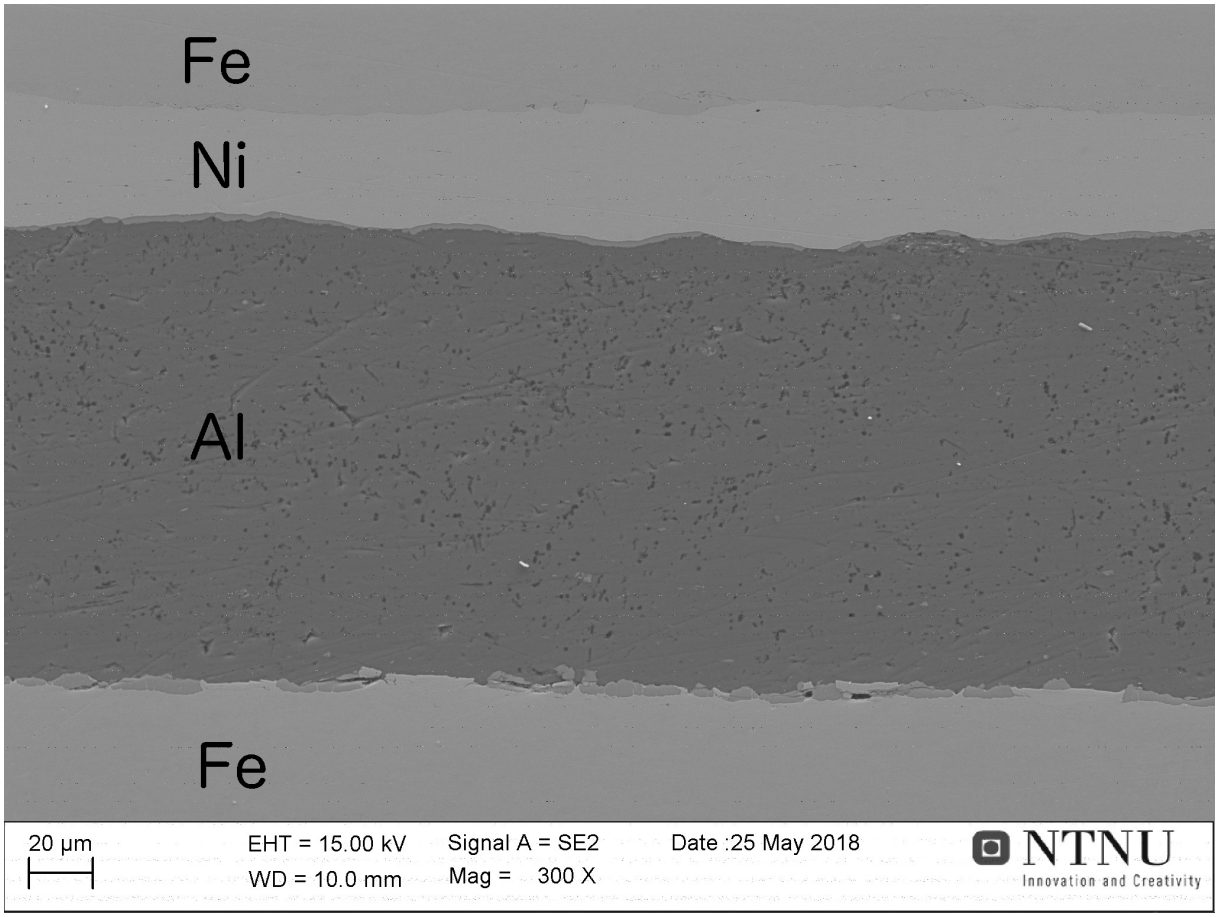

Figure 30: SEM cross-sectional overview image of sample heat-treated at $450°C$ for $1hour$.

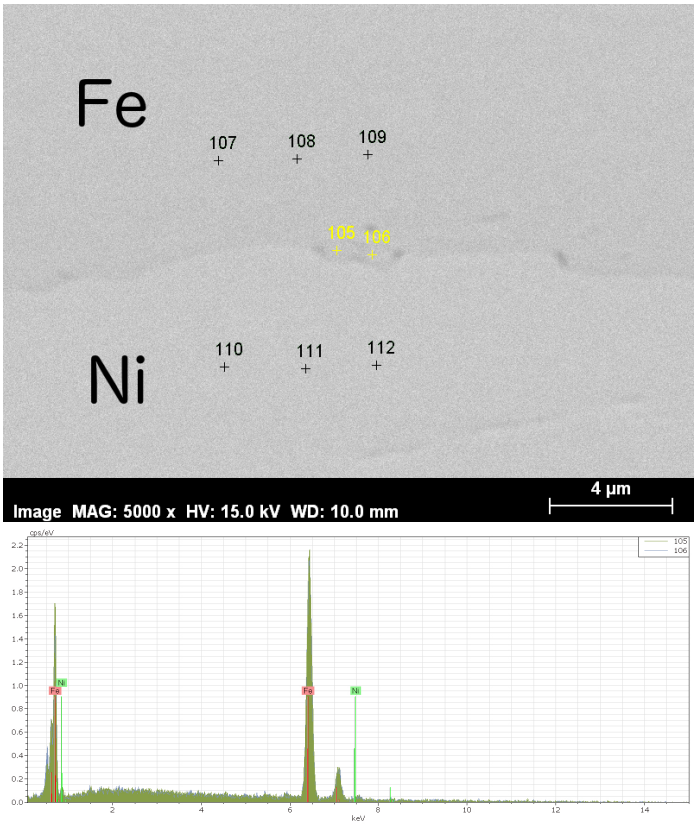

Figure 31: EDS point scans at Fe-Ni interface of sample heat-treated at 450°C for 1$hour$ reveal that the particles present are in fact steel.

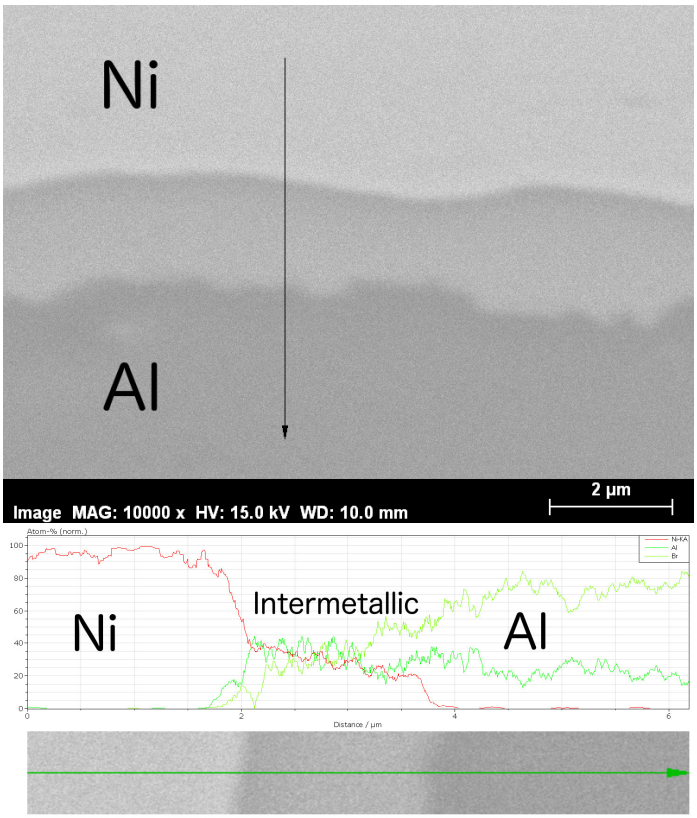

Figure 32: EDS line scan at Al-Ni interface of sample heat-treated at 450°C for 1$hour$.

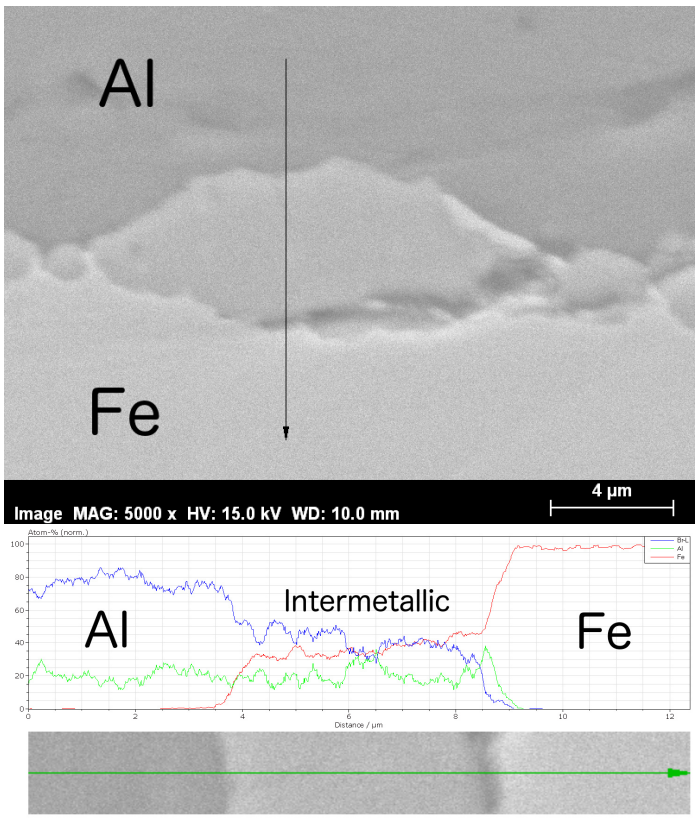

Figure 33: EDS line scan at Al-Fe interface of sample heat-treated at $450°C$ for $1hour$.

Figure 34 shows a cross-sectional overview of the sample heated at $400°C$ for $1hour$. The overview image shows no sign of intermetallics on the steel-aluminium interface, nor on the aluminium-nickel interface. The steel-nickel interface is characterised by huge cracks and large particles.

Figure 35 shows EDS scan across the steel-nickel interface. The huge particles with cracks running on both sides were identified as nickel particles. Figure 36 shows steel-aluminium and aluminium-nickel interfaces at an closer inspection. One intermetallic phase is present at each of the interfaces, too thin to quantify by EDS (due to the electron interaction volume).

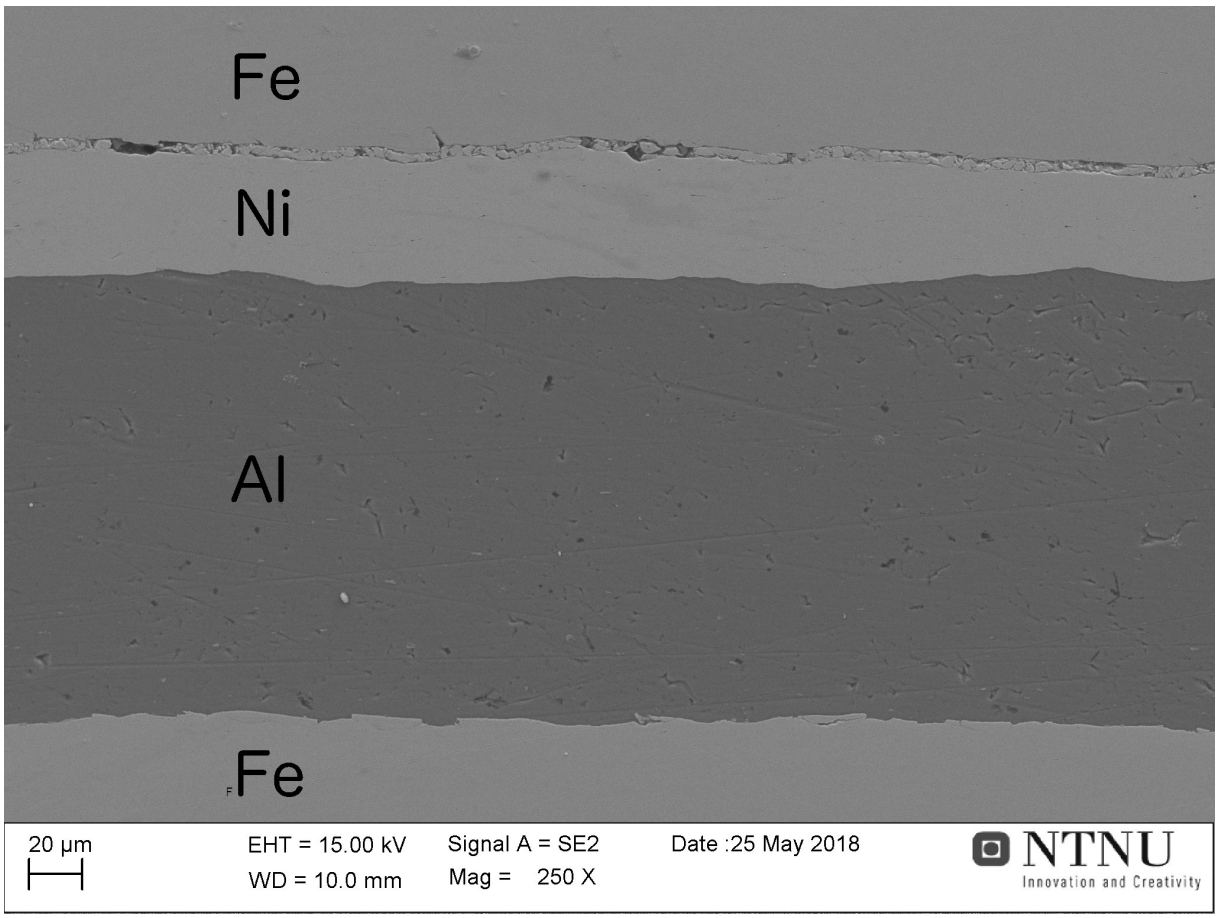

Figure 34: SEM cross-sectional overview image of sample heat-treated at $400°C$ for $1hour$, showing all layers.

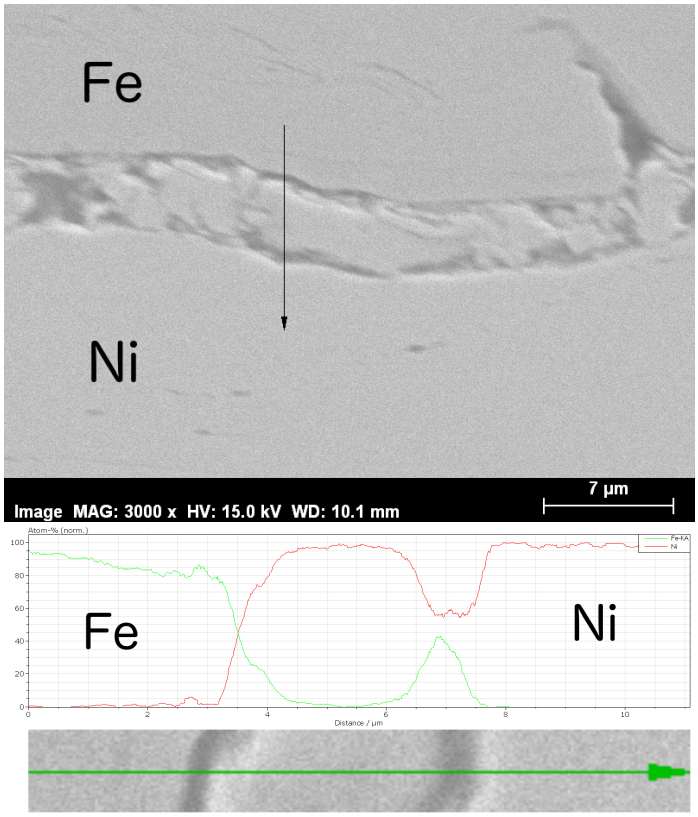

Figure 35: EDS line scan at Fe-Ni interface of sample heat-treated at $400°C$ for $1hour$.

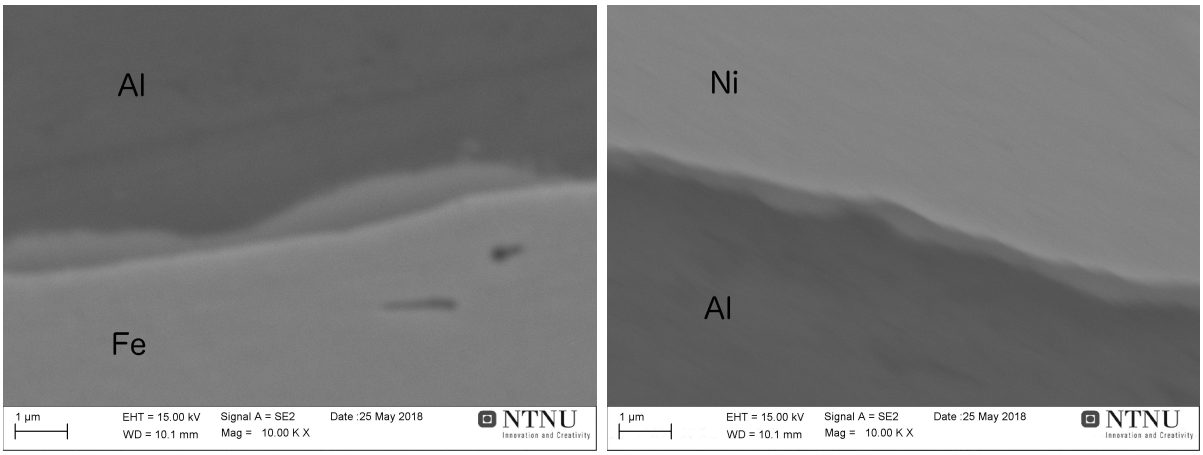

(a) **(b)**

Figure 36: SEM images of sample heat-treated at $400°C$ for $1hour$. **(a)** Fe-Al interface with a visible intermetallic layer. **(b)** Al-Ni interface with a visible intermetallic layer. Both layers too thin to quantify by EDS due to the large electron interaction volume.

5 Discussion

5.1 The effect of brushing direction

There is no distinct difference between surfaces of samples brushed in the transverse direction and those brushed in the rolling direction. Surfaces look similar, only the orientation varies. As for the peel-test results, samples produces with brushing in TD obtained slightly higher values than those brushed in RD but with larger deviation of the data.

Error bars, i.e. standard deviations, for the peel tests are high, meaning that there are large variations on the bond qualities on the surface. Degree of deformation is assumed constant for each individual specimen as the rollers are kept steady during rolling. Varying bond strengths can be caused by fluctuating pressure applied by the operator during wire-brushing, by locally contaminating particles etc., or by other means that influence the roll-bonding process. Due to the relatively high deviations, one should read the results with care.

5.2 Fractografic studies

Fractography shows residual material pieces on AA1080-355 and AA1080-316 samples (Figures 17 and 19), however samples produces with a nickel interlayer show almost no residual elements on the fractured surfaces (Figure 21). Dimples on a fractured surface indicates ductile behaviour with the metal deforming plastically before fracturing completely. In order for the aluminium to deform prior to fracture, sound bonds have to be made. Thus, residual aluminium is an indication of the formation of metallurgical bonds between aluminium and steel, bonds with better fracture resistance than the aluminium itself.

Residual steel pieces on aluminium surface indicate sound metallurgical bonds as well. The measured bond strengths are, however, not sufficient high to believe that steel have fractured exclusively as a result of peeling. Size and shape of residual steel pieces, as well as peel strengths measured, indicate that residual steel is in fact loosened particles from pre-rolling brushing. The severe deformation and work hardening of the steel surfaces during brushing is believed to have made the steel brittle and introduced cracks. This explains both residual steel pieces on aluminium and steel particles found between steel and nickel on heat-treated samples, and is in accordance with film theory [30–32].

Fractografic studies are supported by peel test results (Figure 37). Measurements show bond strength of approximate $4 - 12 N/mm$ for the series *without* nickel interlayer and values of approximate $2 - 3 N/mm$ for samples *with* nickel interlayer. Fracture surfaces of 355- and 316-series show metallurgical bonding (residual steel and aluminium) whereas $355Ni$-series show almost no sign of metallurgical bonding at all. Increasing degree of metallurgical bonding is thus found to correlate with increasing bond strength.

Bending (i.e. plastic deformation) of steel contributes to the measured peel-strength and should thus be subtracted from the reported value. However, the magnitude of the contribution is unknown. Specimens with mono-layer steel was rolled to simulate roll-

bonding and dragged through the peel-test rig in order to try to gain an idea of the contribution. The results are presented in Appendix 3. Findings indicate that there is no significant difference between the 355- and 316-steels when it comes to bending upwards. Two samples of each steel type was produced, and the results were $5,2 N/mm$ and $5.3 N/mm$ for 355 and 316L respectively. However, there is a trend when it comes to specimen thickness. The thickest specimen of each steel type resulted in the highest recorded peel-strength, which is in good accordance with classic beam theory. It is suggested that elastic modulus and second moment of area (i.e. E and I respectively) contribute to errors in peel-strength testing. Thus, peel strengths below approximate $5 N/mm$ should be considered *not* bonded.

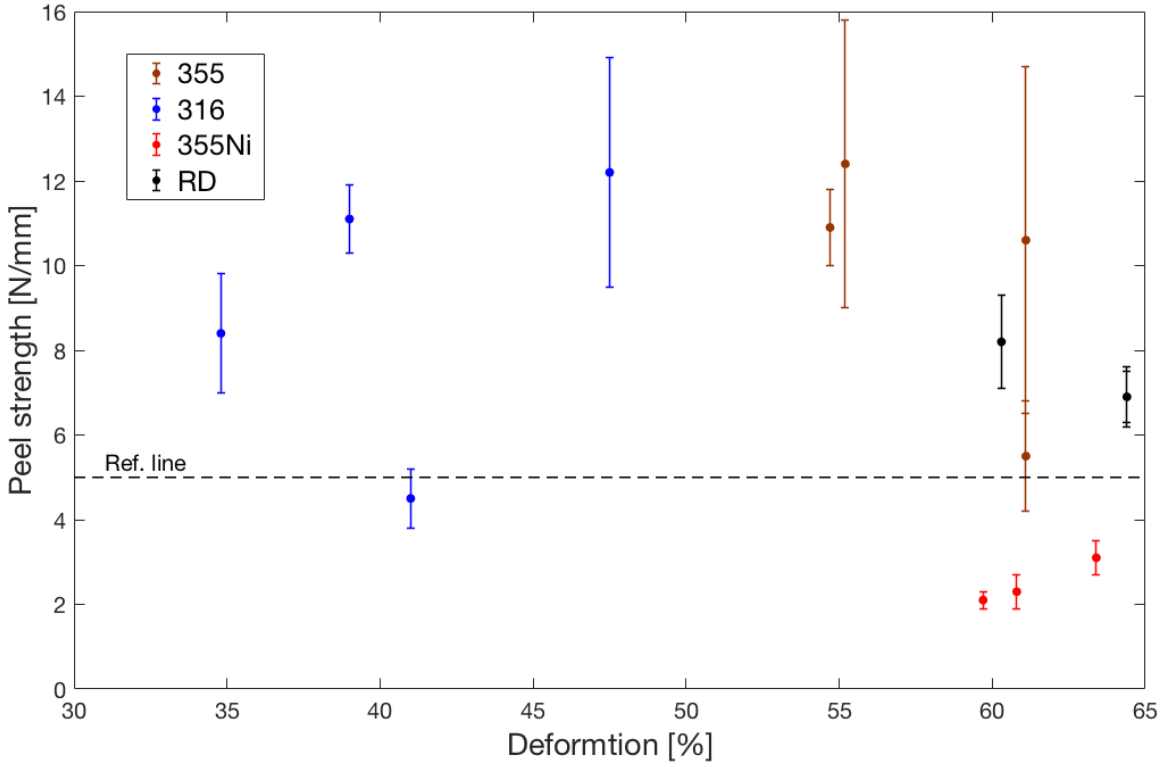

Figure 37: Peel test results from all samples with standard deviation displayed as error bars, plotted as a function of total sample deformation. Note how the stainless steel experienced the least degree of deformation (blue) and samples with nickel interlayer peeled the easiest (red). A reference line with peel strength equal $5 N/mm$ is plotted as a dashed line. Values beneath and/or close to this line can be assumed to not not have bonded.

5.3 Mechanical behaviour of metals

Hardness tests show that both steel types 355 and 316 experienced net work hardening during the roll-bonding process, as expected. Aluminium rolled with 355-steel experienced net recovery, both static and dynamic, whereas aluminium rolled with 316-steel had a break-even hardening/softening process. The aluminium was found to undergo static recovery during pre-heating at $150°C$ in combination with both steel types, thus it can be concluded that the aluminium hardened during roll-bonding with 316-steel.

The fact that aluminium could undergo net recovery means that it was not in an annealed state as received, but in a cold-rolled condition.

5.4 Intermetallic layers

Intermetallic layer thicknesses produced in this report range from non-existing on sample heat-treated at $450°C$ for $1min$ to $16.1\mu m$ for Al-Ni-intermetallics on sample heat-treated at $550°C$ for $1hour$. Intermetallics in the Al-Ni binary system are thinner than the one observed in the Fe-Al binary system at low temperatures and times, but grow larger at higher temperatures. Two distinct intermetallic phases can be seen in the Al-Ni system for samples heat-treated at temperatures higher than $450°C$.

5.4.1 Fe-Al interface

Fe-Al intermetallic phases have fluctuating thicknesses, and for samples heat-treated at $400°C$ and $450°C$ the layers are discrete.

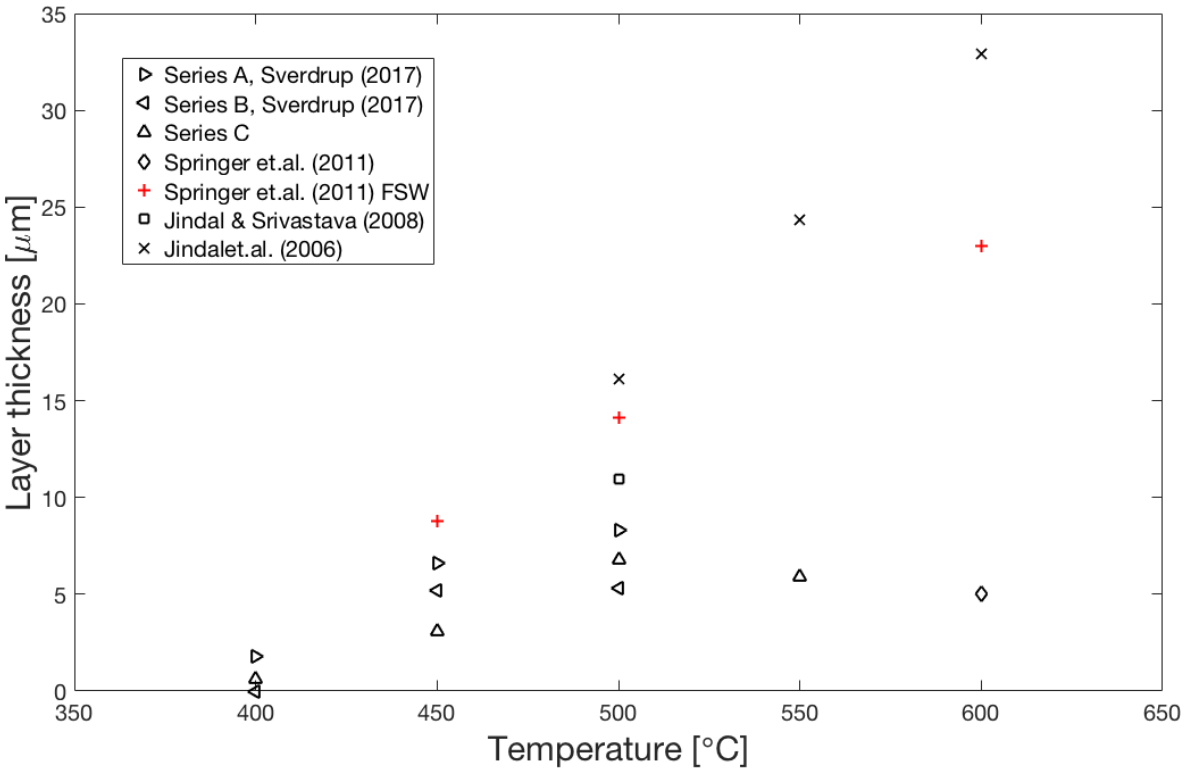

Figure 38: Intermetallic layer thickness in Fe-Al binary system as function of temperature. All samples heat-treated for $1hour$. Graph also includes results from previous project by the author [42], results from Jindal *et al.* [8], Jindal & Srivastava [9] and Springer *et al.* [43, 44]. Note that Springer *et al.* [44] used friction stirred welding (FSW) as bonding method instead of roll-bonding, and the values are thus coloured red.

Figure 38 shows intermetallic phase thickness in the Fe-Al binary system for this report

and selected values from literature. All samples are heat-treated for $1hour$. Values from this report (and previous report by the author) are lower than those from literature. The general trend is increasing layer thickness as the temperature increases, in good accordance with theory [8].

EDS scans of Fe-Al intermetallics does not match exact with the stoichiometry of the known intermetallic phases, and estimates can not be trusted based on the results. However, results indicate formation of a aluminium-rich phase which is in accordance with theory and findings in presented literature [8–10, 16, 43].

5.4.2 Al-Ni interface

EDS line scans across the aluminium-nickel interfaces on samples heat-treated at different temperatures points towards the formation of binary phases Al_3Ni_2 and AlNi. EDS scans indicate that the phase formed after heat-treatment at $400 - 450°C$ had a composition of approximate $Al_{0,6}Ni_{0,4}$, in which case is the composition of Al_3Ni_2. Samples heat-treated at $500 - 550°C$ grew two intermetallics with compositions of approximate $Al_{0,6}Ni_{0,4}$ and $Al_{0,5}Ni_{0,5}$, which corresponds well with Al_3Ni_2 and AlNi, respectively. Figure 39 shows the evolution of the two phases at elevating temperatures.

Theory states that the first phase to form should be Al_3Ni with Al_3Ni_2 growing thereafter [16]. Literature presented states the formation of these phases [20], but this report indicates otherwise. Based on this observation, and observation from the steel-aluminium intermetallic, EDS scans were not fully trusted to base exact stoichimetric quantification upon, only qualitative conclusions were drawn.

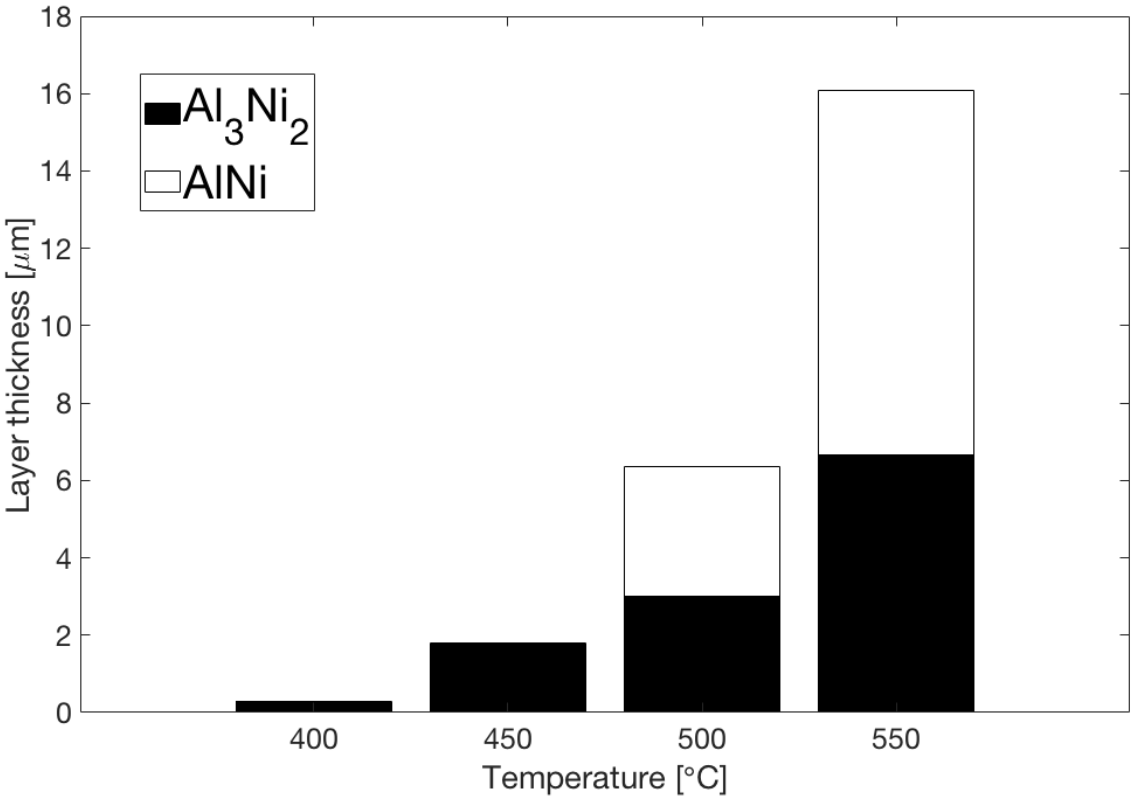

Figure 39: Thickness of intermetallic layers in the Al-Ni binary system. Note that the phases are not fully trusted to be correct, only indicated.

Both phases Al_3Ni_2 and AlNi seem to grow with an parabolic temperature-dependency.

5.4.3 Growth kinetics

If the temperature varies with time, i.e. $T = f(t)$, Equation 9 does not have an analytical solution and thus has to be solved numerically. However, by assuming that the heating and cooling rates are infinite fast and holding temperature constant, temperature can be assumed time-independent. Equation 9 can thus be simplified to

$$\Delta x = \left[2k_0 \exp\left(\frac{-Q}{RT}\right) t \right]^{1/2} \tag{12}$$

These assumptions are justified by the heat-treatment procedure chosen in this thesis. Samples were immersed in pre-heated salt baths with a size relatively large compared to the sample dimensions, and kept for the demanded time. After heating the samples were quenched and stirred in room-tempered water to quickly obtain room temperature.

Curve fitting was conducted on Equation 12 by adjusting the pre-exponential constant k_0 and activation energy Q to fit the experimental results. Results from the modelling are presented in Table 13, and also shown in Figure 40.

Table 13: Q and k_0 values for best fitted curves for intermetallic growth in Fe-Al and Al-Ni binary systems.

Binary system/assumed phase	$Q\ [\frac{J}{mol}]$	$k_0\ [\frac{\mu m^2}{s}]$
Fe-Al-system	56.270	2.6×10^1
Al_3Ni_2	134.200	2.0×10^6
AlNi	276.280	4.3×10^{15}

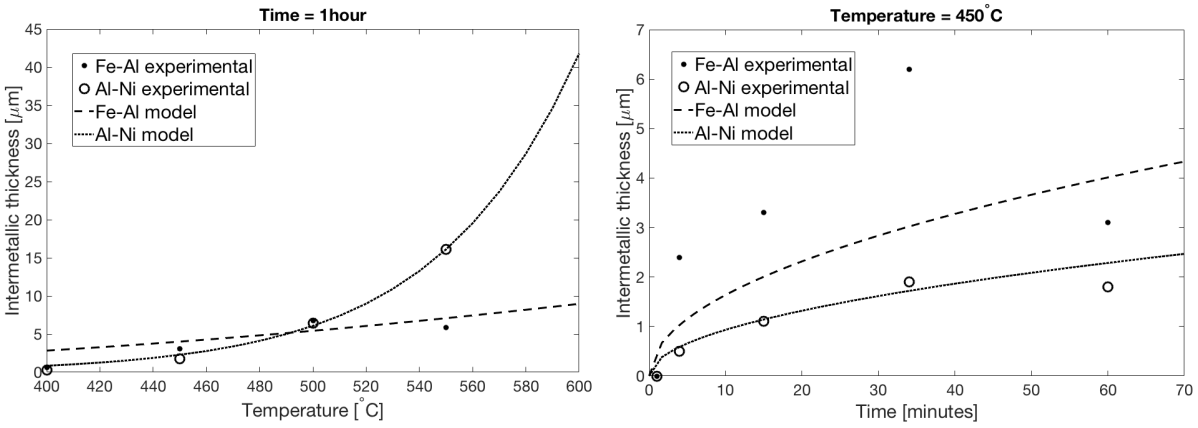

(a) **(b)**

Figure 40: Experimental results and modelled values for intermetallic layer thickness in Fe-Al and Al-Ni binary systems as a function of **(a)** temperature and **(b)** time.

The activation energy for intermetallic growth in the Fe-Al binary system was found to be approximate $56kJ/mol$, which is below results from literature. Jindal *et al.* [8] reported that $Q = 85kJ/mol$, Springer *et al.* [43] reported that $Q = 190kJ/mol$, Wang & Vecchio [19] reported that $Q = 150kJ/mol$ and Xu *et al.* [45] reported that $Q = 160kJ/mol$, all on the solid-solid formation of Fe_2Al_5. Low activation energy can be explained by the low carbon content in the steel ($C_{eq} = 0.18wt\%$) and high purity of aluminium ($\geq 99.8\%$).

Activation energies for the Al-Ni system match well with those found in literature. Adabi & Amadeh [13] found that $Q = 62kJ/mol$, Jain & Gupta [46] found that $Q = 165kJ/mol$ and Ren *et al.* [47] found that $Q = 99kJ/mol$, all for the Al_3Ni_2 phase.

The pre-exponential constant k_0 varies a lot more on the other hand. Best fit was obtained with $k_0 = 2.6 \times 10^1 \frac{\mu m^2}{s}$ for the Fe-Al binary system, $k_0 = 2.0 \times 10^6 \frac{\mu m^2}{s}$ for Al_3Ni_2 and $k_0 = 4.3 \times 10^{15} \frac{\mu m^2}{s}$ for AlNi. Jindal *et al.* [8] found k_0 to be in the order of $10^4 \frac{\mu m^2}{s}$.

5.4.4 Interlayer crack formation and Kirkendall-porosity

Most heat-treated samples showed cracks running between the aluminium and the Fe-Al-intermetallic layer. Springer *et al.* [44] reported of similar pores/voids in diffusion joined steel-aluminium samples. These may be Kirkendall-pores formed due to differences in diffusion-rates for the metals studied.

6 Conclusion

Cold roll bonded samples of 355-steel and $AA1080$, 316-steel and $AA1080$, and 355-steel, $AA1080$ and Ni-interlayer were produced, and interface characteristics and fracture surfaces were studied. A heat-treating study was conducted on samples made with 355-steel, $AA1080$ and Ni-interlayer, and intermetallic layer growths were investigated. Activation energies and pre-exponential factors in the parabolic growth rate model was modelled by a best-fit approach.

The thesis can be concluded in following bullet points:

- Wire brushing in transverse or rolling direction showed no significant difference regarding peel-strength or surface topology for this study. Thus, it is recommended that the operator does what is most convenient, which in the case of this study was brushing in transverse direction.
- Samples produced *without* nickel interlayer fractured by ductile behaviour in aluminium at the steel-aluminium interface, leaving residual aluminium on the steel surface. Residual steel was found on the aluminium surfaces but is believed to have fractured mainly during pre-rolling wire brushing. All samples showed sign of metallurgical bonding, which was supported by peel tests. Samples produced *with* nickel interlayer on the other hand fractured on the steel-nickel interface with no sign of metallurgical bonding.
- Intermetallic phases were not successfully quantified, but EDS scans indicate that all phases are in the aluminium-rich part of their respective binary systems. This is in accordance with theory and presented literature.
- The parabolic growth rate model gives a fair estimate of the intermetallic layer thicknesses. Activation energies was found to be $56kJ/mol$, $134kJ/mol$ and $276kJ/mol$ for Fe-Al system, Al_3Ni_2 and AlNi respectively.
- Fractographic studies and cross-sectional imaging showed that bonding was in good accordance with the film theory for all steel-aluminium samples produced. Both steel types had discrete sites of residual aluminium, indicating that cracks were opened and virgin metal extruded at those sites, as stated by the film theory.
- Steels, both low-alloyed and stainless, experienced net work hardening, whereas aluminium experienced net recovery (roll-bonded with 355-steel) or break-even (roll-bonded with 316-steel) processes.

7 Further work

This chapter presents suggested exercises to continue the field of study started by this thesis.

Material selection: Although commercial pure aluminium has its benefits (e.g. easy to work, easy to grow intermetallic phases) it clearly has its disadvantages (e.g. weak, soft). By changing to a stronger aluminium alloy (e.g. 6xxx- or 7xxx-series), the roll-bonded laminates produced are more versatile regarding mechanical applications.

Intermetallic phase quantification: As EDS was not sufficient to quantify intermetallic phases it is suggested to utilise more powerful tools such as Transmission Electron Microscopy (TEM), Electron Backscatter Diffraction (EBSD) and/or X-ray crystallography. TEM was successfully used by Springer *et al.* [43] to quantify intermetallic phases in steel-aluminium binary systems, as well as steel-aluminium-silicon ternary systems.

Peel test of heat-treated samples: In this report, roll-bonded samples were peel-tested without being heat-treated, thus testing peel strength of welds without intermetallic phase(s) present. Strength of the intermetallic layers could be tested by heat-treating the samples prior to peel-testing. This is highly interesting for samples with Ni-interlayer as they showed no sign of welding as-rolled.

References

1. Ashby, M. F. *Materials Selection in Mechanical Design.* (Elsevier Ltd, 2011).
2. Solberg, J. K. *Teknologiske metaller og legeringer* nor (Institutt for materialteknologi, Norges teknisk-naturvitenskapelige universitet, Trondheim, 2014).
3. *Aluminum Alloys 101* `http://www.aluminum.org/resources/industry-standards/aluminum-alloys-101`. (accessed: 14.05.2018).
4. Dieter, G. E. *Mechanical metallurgy* eng (McGraw-Hill, 1988).
5. Callister, W. D. *Materials science and engineering* 8th ed., SI version. eng (Wiley, 2011).
6. Bhadeshia, H. K. D. H. *Steels : microstructure and properties* 3rd ed. eng (Elsevier, Amsterdam, 2006).
7. Humphreys, F. & Hatherly, M. in *Recrystallization and Related Annealing Phenomena (Second Edition)* 169–213 (Elsevier, Oxford, 2004).
8. Jindal, V., Srivastava, V., Das, A. & Ghosh, R. Reactive diffusion in the roll bonded iron-aluminum system. *Materials Letters* **60,** 1758–1761 (2006).
9. Jindal, V. & Srivastava, V. Growth of intermetallic layer at roll bonded IF-steel/aluminum interface. *Journal of Materials Processing Technology* **195,** 88–93 (2008).
10. Jindal, V., Srivastava, V. C. & Ghosh, R. N. Development of IF steel–Al multilayer composite by repetitive roll bonding and annealing process. *Materials Science & Technology* **24,** 798–802 (2008).
11. Kobayashi, S. & Yakou, T. Control of intermetallic compound layers at interface between steel and aluminum by diffusion-treatment. *Materials Science and Engineering: A* **338,** 44–53 (2002).
12. Massalski, T. B. *Binary alloy phase diagrams* 2nd ed. eng (ASM International, 1990).
13. Adabi, M. & Amadeh, A. A. Formation mechanisms of Ni–Al intermetallics during heat treatment of Ni coating on 6061 Al substrate. *Transactions of Nonferrous Metals Society of China* **25,** 3959–3966 (2015).
14. Bené, R. W. First nucleation rule for solid-state nucleation in metal-metal thin-film systems. *Applied Physics Letters* **41,** 529–531 (1982).
15. Pretorius, R. Phase sequence of silicide formation at metal-silicon interfaces. *Vacuum* **41.** Selected proceedings of the 11th international vacuum congress (IVC-11) 7th international conference on solid surfaces (ICSS-7), 1038–1042 (1990).
16. Pretorius, R., Marais, T. & Theron, C. Thin film compound phase formation sequence: An effective heat of formation model. *Materials Science Reports* **10,** 1–83 (1993).
17. Pretorius, R., Vredenberg, A. M., Saris, F. W. & de Reus, R. Prediction of phase formation sequence and phase stability in binary metal-aluminum thin-film systems using the effective heat of formation rule. *Journal of Applied Physics* **70,** 3636–3646 (1991).
18. Theron, C., Ndwandwe, O., Lombaard, J. & Pretorius, R. First phase formation at interfaces: Comparison between Walser-Bené and effective heat of formation model. *Materials Chemistry and Physics* **46,** 238–247 (1996).

19. Wang, Y. & Vecchio, K. S. Microstructure evolution in Fe-based-aluminide metallic-intermetallic laminate (MIL) composites. *Materials Science and Engineering: A* **649,** 325–337 (2016).

20. Chrifi-Alaoui, F., Nassik, M., Mahdouk, K. & Gachon, J. Enthalpies of formation of the Al–Ni intermetallic compounds. *Journal of Alloys and Compounds* **364,** 121–126 (2004).

21. Laik, A., Bhanumurthy, K. & Kale, G. Intermetallics in the Zr-Al diffusion zone. *Intermetallics* **12,** 69–74 (2004).

22. Thirunavukarasu, G., Kundu, S., Mishra, B. & Chatterjee, S. Effect of Bonding Time on Interfacial Reaction and Mechanical Properties of Diffusion-Bonded Joint Between Ti-6Al-4V and 304 Stainless Steel Using Nickel as an Intermediate Material. *Metallurgical and Materials Transactions A* **45,** 2078–2090 (2014).

23. Thirunavukarasu, G., Kundu, S., Mishra, B. & Chatterjee, S. Effect of Bonding Temperature on Interfacial Reaction and Mechanical Properties of Diffusion-Bonded Joint Between Ti-6Al-4V and 304 Stainless Steel Using Nickel as an Intermediate Material. *Metallurgical and Materials Transactions A* **45,** 2067–2077 (2014).

24. Kundu, S. & Chatterjee, S. Mechanical properties of diffusion bonded joints between titanium and stainless steel with nickel interlayer. *Materials Science and Technology* **23,** 1167–1172 (2007).

25. Kundu, S. & Chatterjee, S. Characterization of diffusion bonded joint between titanium and 304 stainless steel using a Ni interlayer. *Materials Characterization* **59,** 631–637 (2008).

26. Yıldız, A., Kaya, Y. & Kahraman, N. Joint properties and microstructure of diffusion-bonded grade 2 titanium to AISI 430 ferritic stainless steel using pure Ni interlayer. *The International Journal of Advanced Manufacturing Technology* **86,** 1287–1298 (2016).

27. Zhong, Z., Hinoki, T. & Kohyama, A. Effect of holding time on the microstructure and strength of tungsten/ferritic steel joints diffusion bonded with a nickel interlayer. *Materials Science and Engineering: A* **518,** 167–173 (2009).

28. Mori, K.-i., Bay, N., Fratini, L., Micari, F. & Tekkaya, A. E. Joining by plastic deformation. *CIRP Annals* **62,** 673–694 (2013).

29. Wang, C., Jiang, Y., Xie, J., Zhou, D. & Zhang, X. Interface formation and bonding mechanism of embedded aluminum-steel composite sheet during cold roll bonding. *Materials Science and Engineering: A* **708,** 50–59 (2017).

30. Bay, N. Cold pressure welding - the mechanisms governing bonding. *Journal of engineering for industry* **101,** 121–127 (1979).

31. Bay, N. Mechanisms producing metallic bonds in cold welding. *Welding Journal (Miami, Fla)* **62** (1983).

32. Mohamed, H. & Washburn, J. Mechanism of solid state pressure welding. *Welding Journal (Miami, Fla)* (1975).

33. Bay, N., Clemensen, C., Juelstorp, O. & Wanheim, T. Bond Strength in Cold Roll Bonding. *CIRP Annals* **34,** 221–224 (1985).

34. Jamaati, R. & Toroghinejad, M. R. The Role of Surface Preparation Parameters on Cold Roll Bonding of Aluminum Strips. *Journal of Materials Engineering and Performance* **20,** 191–197 (2011).

35. Valberg, H. *Applied metal forming : including FEM analysis* eng. Cambridge, 2010.

36. *ASTM-D1876-08, Standard Test Method for Peel Resistance of Adhesives* https://compass.astm.org/EDIT/html_annot.cgi?D1876+08(2015)e1. (accessed: 30.05.2018).

37. *ASTM-D3167, Standard Test Method for Floating Roller Peel Resistance of Adhesives* https://compass.astm.org/EDIT/html_annot.cgi?D3167+10(2017). (accessed: 30.05.2018).

38. Hjelen, J. *Scanning elektron-mikroskopi* nor (SINTEF, Trondheim, 1989).

39. Solhaug, H. Thermomechanical processing of an AA6082 - IF steel cold roll bonded composite material. *Master's Thesis NTNU* (2017).

40. Wu, B., Li, L., Xia, C., Guo, X. & Zhou, D. Effect of surface nitridingtreatment in a steel plate on the interfacial bonding strength of the aluminum/steel clad sheets by the cold roll bonding process. *Materials Science and Engineering: A* **682,** 270–278 (2017).

41. *X-ray energies* https://www.bruker.com/fileadmin/user_upload/8-PDF-Docs/X-rayDiffraction_ElementalAnalysis/HH-XRF/Misc/Periodic_Table_and_X-ray_Energies.pdf. (accessed: 22.05.2018).

42. Sverdrup, E. Controlled growth of intermetallic phases in heat-treated steel-aluminium joinings. *Project work, NTNU - INTERNAL PAPER* (2017).

43. Springer, H. *et al.* On the formation and growth of intermetallic phases during interdiffusion between low-carbon steel and aluminum alloys. eng. *Acta Materialia* **59,** 1586–1600 (2011).

44. Springer, H., Kostka, A., Dos Santos, J. & Raabe, D. Influence of intermetallic phases and Kirkendall-porosity on the mechanical properties of joints between steel and aluminium alloys. eng. *Materials Science & Engineering A* **528,** 4630–4642 (2011).

45. Xu, L., Robson, J. D., Wang, L. & Prangnell, P. B. The Influence of Grain Structure on Intermetallic Compound Layer Growth Rates in Fe-Al Dissimilar Welds. *Metallurgical and Materials Transactions A* **49,** 515–526 (2018).

46. Jain, M. & Gupta, S. Formation of intermetallic compounds in the Ni–Al–Si ternary system. *Materials Characterization* **51,** 243–257 (2003).

47. Ren, X., Chen, G., Zhou, W., Wu, C. & Zhang, J. Formation and growth kinetics of intermediate phases in Ni-Al diffusion couples. *Journal of Wuhan University of Technology-Mater. Sci. Ed.* **24,** 787 (2009).

8 Appendices

8.1 Appendix 1: Tensile test results

Table 14: Tensile test results for AA1080 and 355 MC.

Specimen ID	Yield stress $[MPa]$	Yield strain $[\frac{mm}{mm}]$	Ultimate tensile strength $[MPa]$
355 MC 1	173,5	0,00754	348,2
355 MC 2	175,0	0,00751	350,6
AA1080 1	112,6	0,00346	119,8
AA1080 2	112,7	0,00477	120,4

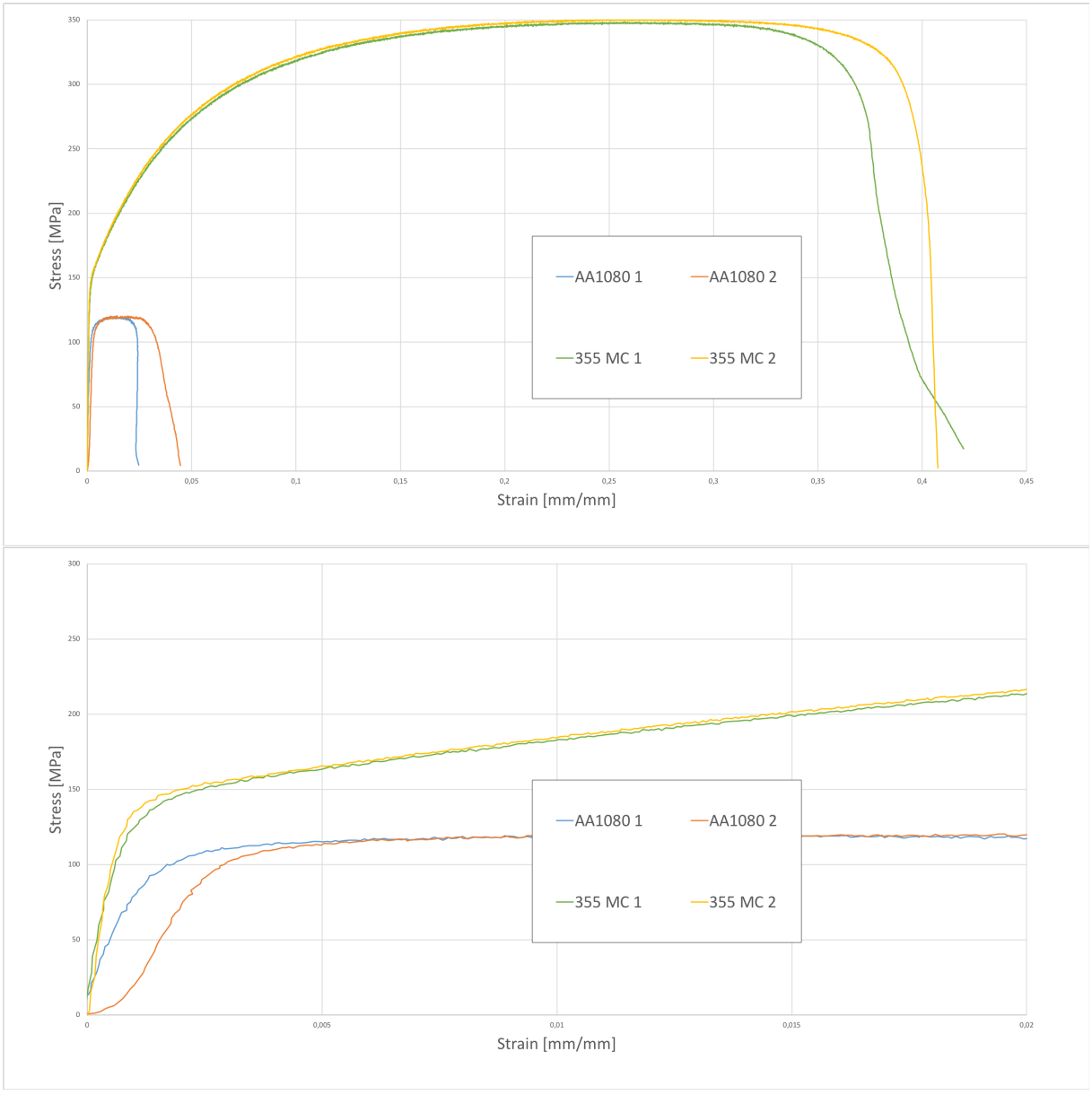

Figure 41: Tensile test result plots. Top image shows whole test. Bottom image shows closeup at low strain values.

8.2 Appendix 2: LOM thickness measurements

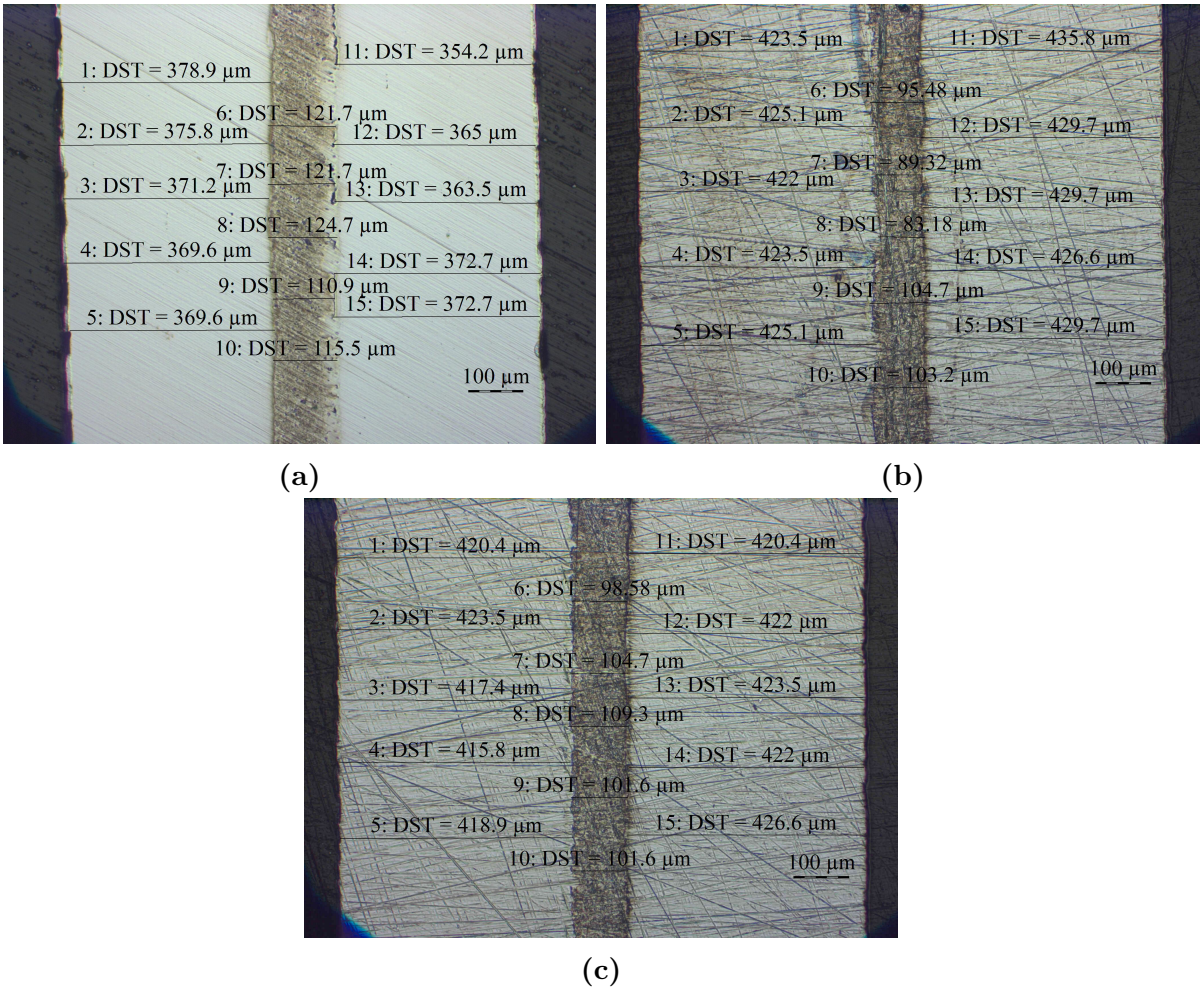

Figure 42: Thickness measurements of samples **(a)** RD_3, **(b)** RD_4 and **(c)** RD_5 post roll-bonding.

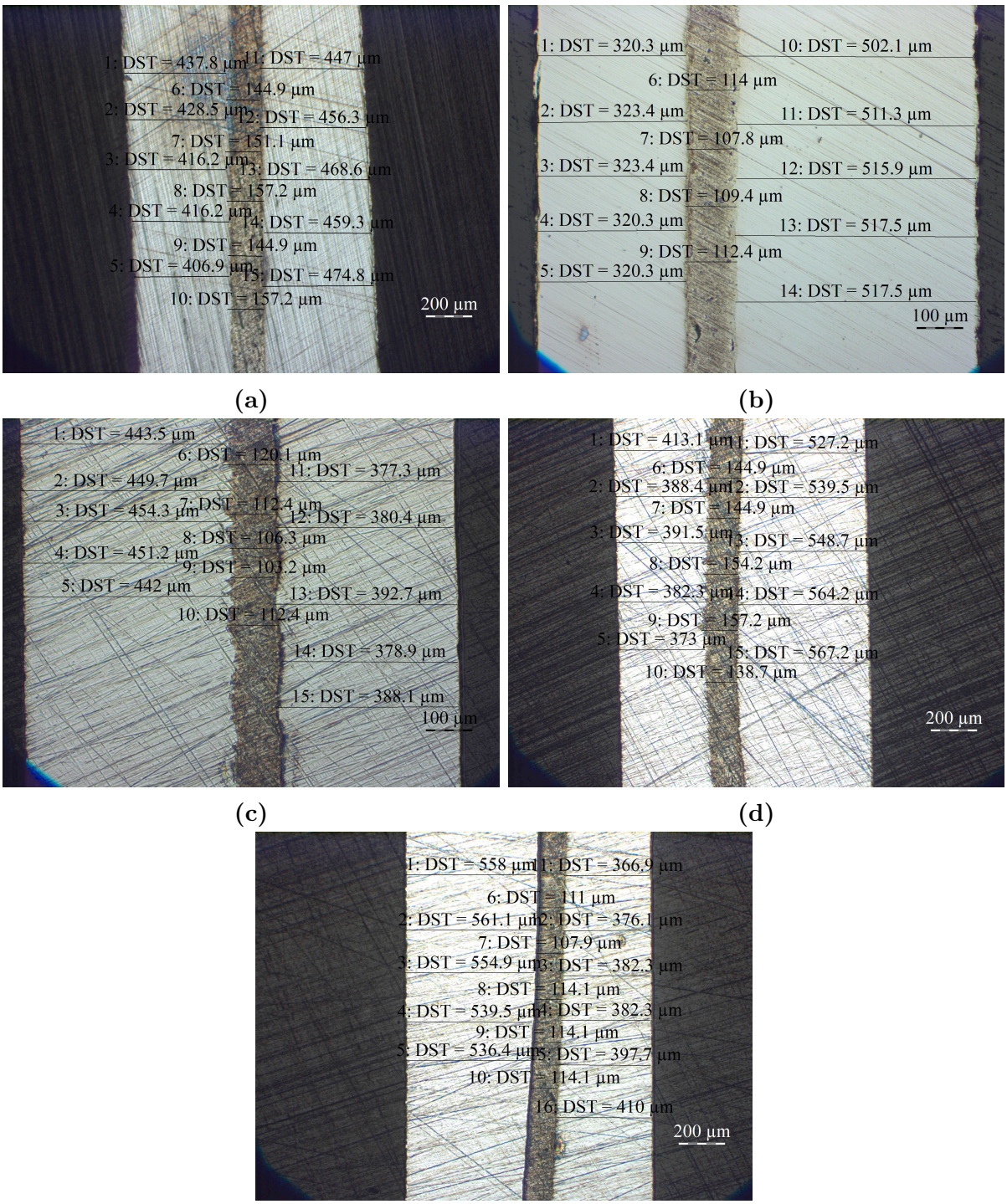

Figure 43: Thickness measurements of samples **(a)** 355_1, **(b)** 355_2, **(c)** 355_3, **(d)** 355_4 and **(e)** 355_5 post roll-bonding.

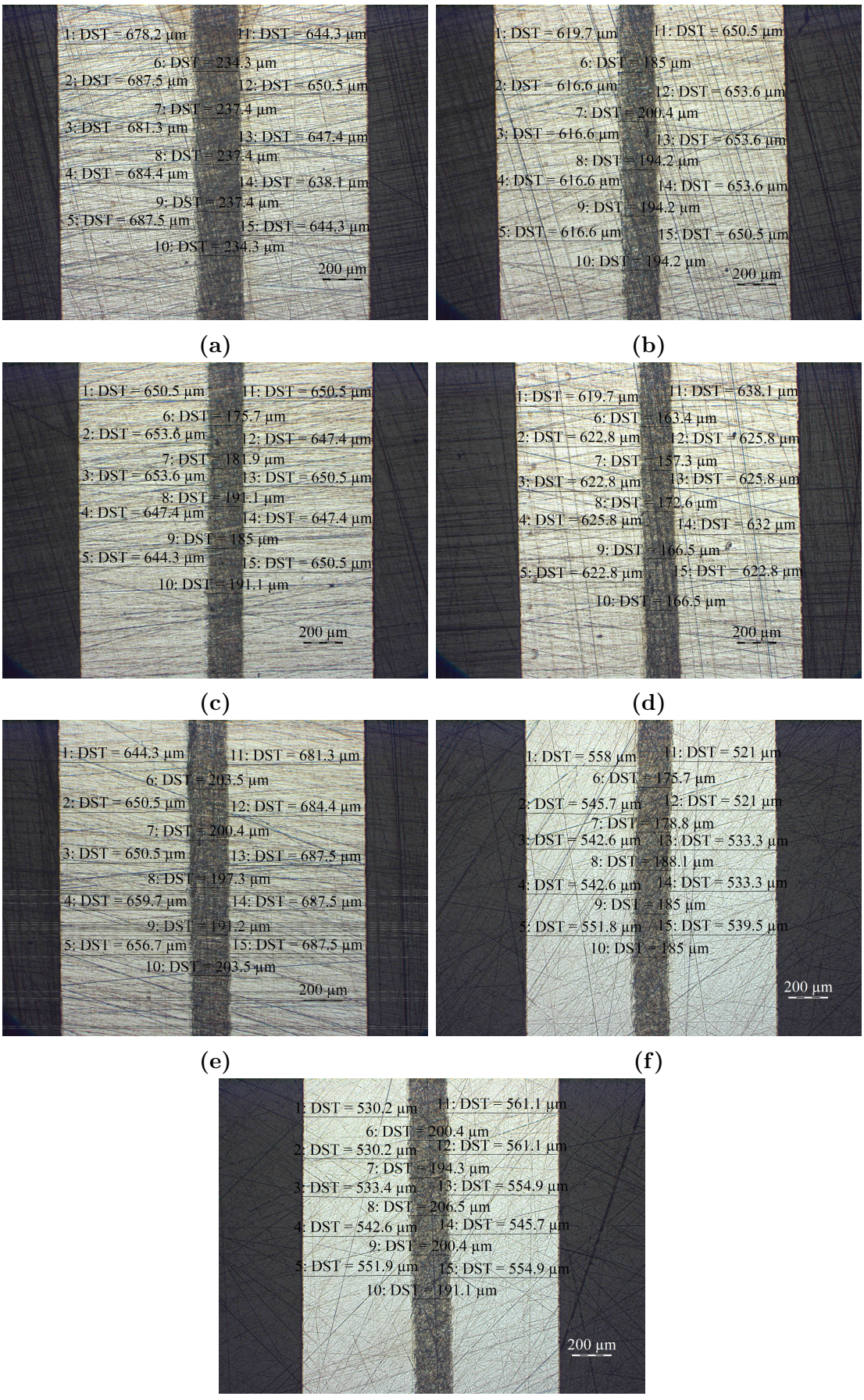

Figure 44: Thickness measurements of samples **(a)** 316_1, **(b)** 316_2, **(c)** 316_3, **(d)** 316_4, **(e)** 316_5, **(f)** 316_6 and **(g)** 316_7 post roll-bonding.

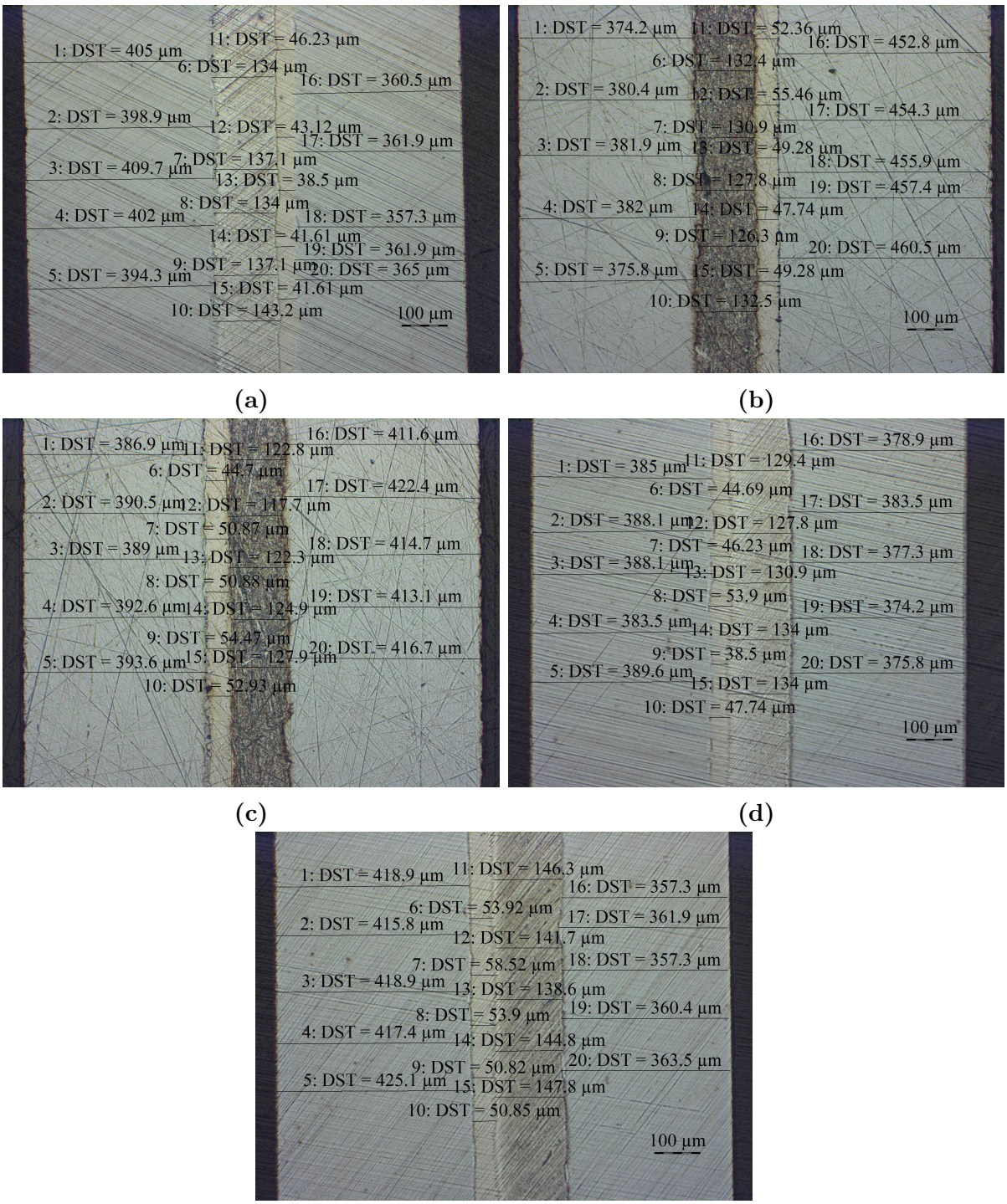

Figure 45: Thickness measurements of samples **(a)** $355Ni_1$, **(b)** $355Ni_2$, **(c)** $355Ni_3$, **(d)** $355Ni_4$ and **(e)** $355Ni_5$ post roll-bonding.

8.3 Appendix 3: Peel-test references

Figure 46 shows peel-test raw data for reference specimens. Average values are obtained by starting $40mm$ from the beginning of the test and ending approximate $20mm$ before the test ended. Table 15 shows the measured post-rolling thickness of the reference specimens as measured with a caliper.

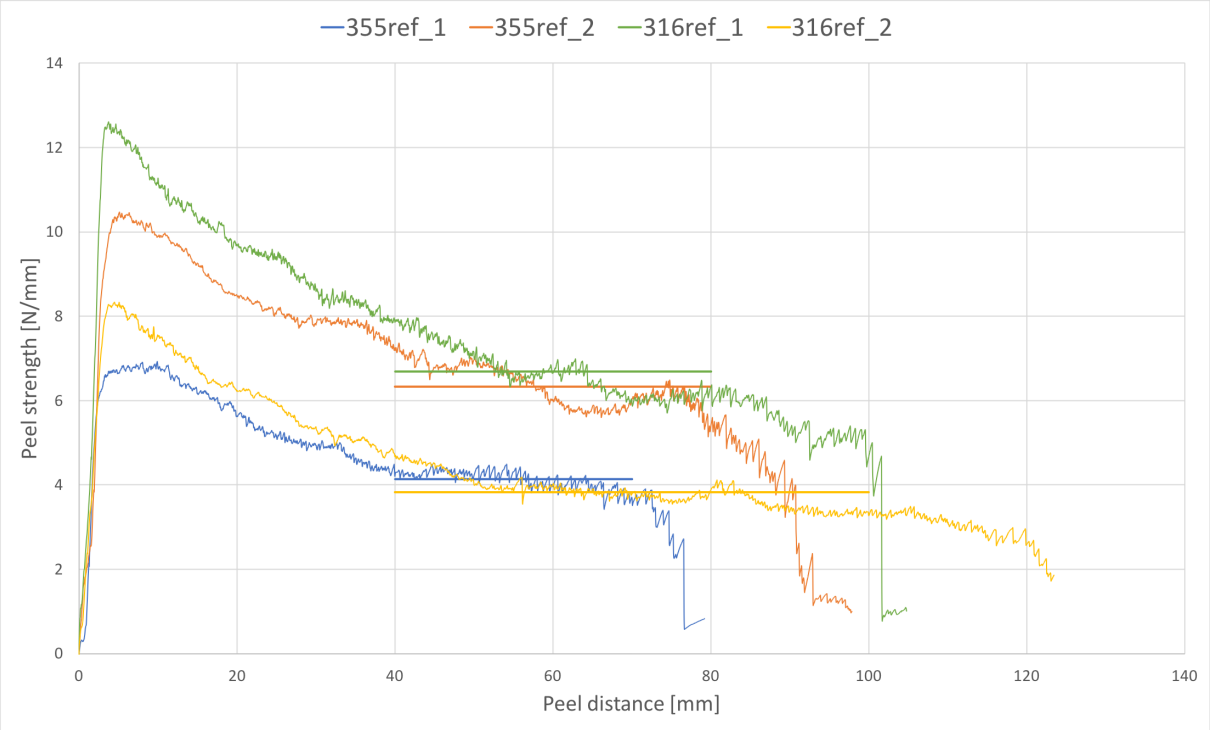

Figure 46: Peel-test reference tests. Tests conducted on single sheet, rolled metal pieces in order to gain an idea of how much of the recorded peel-strength is in fact due to plastic deformation and not the joint. Two tests were conducted on each steel type. Average values were calculated starting at $40mm$. Average values were found to be $5.2 \pm 0.4 \frac{N}{mm}$ and $5,3 \pm 0.8 \frac{N}{mm}$ for $355MC$ and $316L$ respectively.

Table 15: Post-rolling thickness of reference tests

Steel type	Number	Post-rolling thickness $[mm]$
355	1	0.70
	2	0.75
316	1	0.82
	2	0.64

8.4 Appendix 4: 355-steel after initial processing

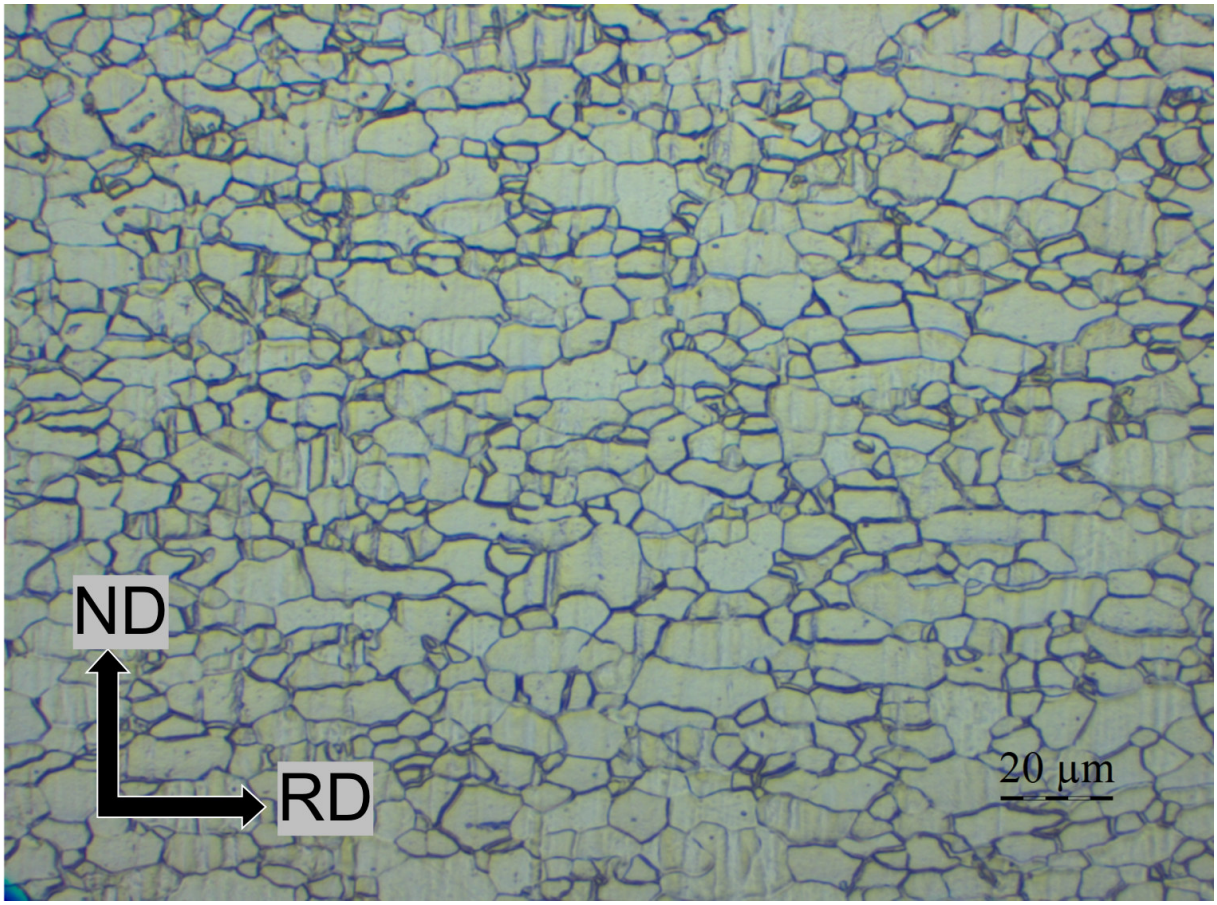

Figure 47: LOM image of 355-steel after initial rolling and heat-treatment. Grains have recrystallised to equiaxed shape.